

## High-Resolution Dual-Doppler Analyses of the 29 May 2001 Kress, Texas, Cyclic Supercell

JEFFREY R. BECK AND JOHN L. SCHROEDER

*Atmospheric Science Group, Texas Tech University, Lubbock, Texas*

JOSHUA M. WURMAN

*Center for Severe Weather Research, Boulder, Colorado*

(Manuscript received 23 August 2005, in final form 13 February 2006)

### ABSTRACT

On 29 May 2001, Doppler on Wheels radars collected data on a supercell near Kress, Texas. The supercellular storm, cyclic in nature, produced multiple mesocyclones throughout its lifetime. Dual-Doppler syntheses were conducted using a grid spacing of 100 m, resulting in the highest-resolution observational analysis of a cyclic supercell to date. In addition, collection of data from ground-based radar allowed for the analysis of near-ground features irresolvable with airborne radar, providing another advantage over previous studies. The syntheses revealed a number of evolving low-level mesocyclones over the observation period of 900 s. While nontornadic during the synthesis period, the supercell exhibited evidence of strong (vertical vorticity greater than  $10^{-2} \text{ s}^{-1}$ ) low-level circulation with classic cyclic structure and multiple tornadoes beginning 3600 s later. A comparison between the current results, conceptual models, and previous lower-resolution analyses is presented. A striking similarity exists between the cyclic evolution of the Kress storm during the synthesis time period and other previous cyclic conceptual models. However, differences did exist between the Kress storm and previously studied tornadic storms. Analysis showed that the rear-flank downdraft provided the only surface boundary associated with low-level mesocyclogenesis. Other characteristics, including forward-flank gust front structure and the orientation of low-level horizontal vorticity, also differed. In addition, there was a general lack of surface convergence associated with the forward-flank reflectivity gradient, yet convergence associated with the forward-flank gust front increased with height. Finally, a large component of crosswise horizontal vorticity was found to exist throughout the supercell environment, within both the inflow and outflow. Incorporating these differences, an attempt was made to identify possible mechanisms responsible for the lack of tornadogenesis during the synthesis time period.

### 1. Introduction

A growing number of studies have shown that supercells can develop a series of discrete mesocyclones throughout their lifetime (Burgess et al. 1982; Johnson et al. 1987; Adlerman et al. 1999; Dowell and Bluestein 2002a,b, hereafter DB02a and DB02b, respectively, or DB for both). With each mesocyclone comes the potential for tornadoes, often resulting in a regular pattern of tornadic development (Darkow and Roos 1970; Darkow 1971; Lemon and Doswell 1979; DB). If a storm develops multiple mesocyclones and/or torna-

does during its lifetime, it is said to be cyclic in nature (Darkow and Roos 1970; DB02a).

A number of early studies (e.g., Darkow and Roos 1970; Darkow 1971) acknowledged visual observational evidence of cyclic tornadogenesis within a single supercell; however, it was not until the advent of Doppler radar that the cyclic nature of mesocyclones within certain supercells was identified. Brandes (1977b) used dual-Doppler syntheses to identify discrete vortices along the rear-flank gust front, but Burgess et al. (1982) were the first to create a conceptual model of cyclic evolution based on Doppler radar data. The Burgess et al. (1982) model (Fig. 1) represents a mesocyclone and rear-/forward-flank gust fronts in a similar manner to that of a classic synoptic cyclone. With the possible exception of the forward-flank gust front, the model has remained relatively unchanged to date and is ref-

---

*Corresponding author address:* Jeffrey R. Beck, Atmospheric Science Group, Department of Geosciences, Texas Tech University, Box 42101, Lubbock, TX 79409.  
E-mail: j.beck@ttu.edu

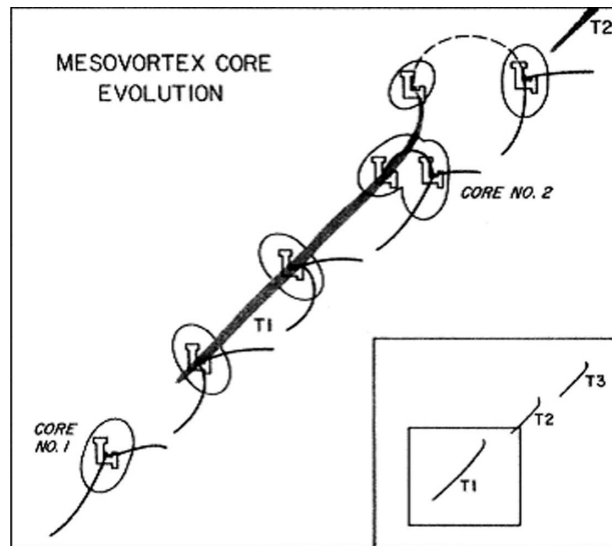


FIG. 1. Conceptual model of cyclic mesocyclogenesis from Burgess et al. (1982). Each discrete mesocyclone is identified with an "L." Rear-flank and forward-flank boundaries are shown using thin lines, while tornado tracks are shaded. The inset within the tornado track summary indicates the area documented within the larger portion of the figure.

erenced and verified in a number of more recent papers including Johnson et al. (1987) and DB.

Brandes (1977b) and Johnson et al. (1987) both conducted dual-Doppler analyses of cyclic supercells using fairly coarse resolution Doppler radar data from traditional stationary radar platforms. However, Wakimoto and Cai (2000) and DB conducted the first dual-Doppler analyses of cyclic supercells in close proximity to a storm using airborne radar, resulting in much finer resolution than any previous dataset. These studies allowed for further, more detailed evaluation of the Burgess et al. (1982) conceptual model. In their study DB found that, for the most part, the model was upheld based on their analyses. However, a few minor exceptions were found. The motion of tornadoes (and therefore low-level mesocyclones) relative to the storm began to move left of the mean flow earlier than displayed in the Burgess et al. (1982) model. Also, forward-flank gust fronts were either absent or very weak. This result indicated that newly developing areas of vorticity had occurred along the rear-flank gust front in absence of any forward-flank wind shift. Taking these exceptions to the earlier model into consideration, a slightly modified conceptual model was produced by DB02b (Fig. 2).

For the most part, observational studies have dominated cyclic supercell research. However, Adlerman et al. (1999) represent the first numerical modeling study to document the dynamics of cyclic processes. With the exception of the forward-flank gust front structure and

the cycling frequency of subsequent mesocyclones, the major findings in Adlerman et al. (1999) are similar to those found in both Lemon and Doswell (1979) and Burgess et al. (1982).

While observational dual-Doppler analyses are often limited in height and resolution, Adlerman et al. (1999) presented detailed analyses of the cyclic process throughout a significant depth of a supercell. Evidence of a midlevel two-celled updraft structure can be seen in Adlerman et al. (1999) as cyclic mesocyclogenesis is in progress, indicating discrete updrafts associated with separate mesocyclones. This result is very similar to the description of successive updraft formation in Lemon and Doswell (1979). However, as described in Adlerman and Droegemeier (2002a), production of a two-celled updraft structure aloft is highly dependent on the forward progression of the rear-flank gust front. DB02a did not find a secondary updraft aloft within the studied McLean, Texas, storm, attributing this finding to a slowly moving rear-flank gust front.

Adlerman and Droegemeier (2002a) also showed that the differing scales of cyclic evolution, both the tornadic and mesocyclonic scales, are very similar in nature. The cyclic nature in Adlerman et al. (1999) was found to correlate well with the higher-resolution cyclic tornadogenesis model study conducted by Adlerman and Droegemeier (2002a). This finding allowed for the legitimate comparison of cyclic tornadogenesis conceptual models (such as that found in DB) to overall cyclic mesocyclogenesis. This result is of particular importance to assessing similarities and differences between cyclic tornadogenesis conceptual models and nontornadic cyclic mesocyclogenesis observed in the current study.

Even though Wakimoto and Cai (2000) and DB conducted high-resolution dual-Doppler analyses of cyclic supercells superior to any previously conducted, use of the airborne radar platform limited the lowest level of synthesis data to  $\sim 500$  m AGL (DB), below which contamination by ground clutter prevented analysis. This limited the ability to assess near-ground dynamic forcing, of particular interest to the development, maintenance, and dissipation of low-level mesocyclones and tornadoes. It also complicated the determination of the lower vertical velocity boundary condition critical to the accurate retrieval of vertical velocity throughout the storm, as well as the calculation of tilting and stretching terms in the vorticity budget.

The dataset used in the current study alleviated these shortcomings and was collected by the Doppler on Wheels (DOW) radars (Wurman et al. 1997; Wurman 2001) on 29 May 2001 near Kress, Texas, providing the first ground-based high-resolution dual-Doppler

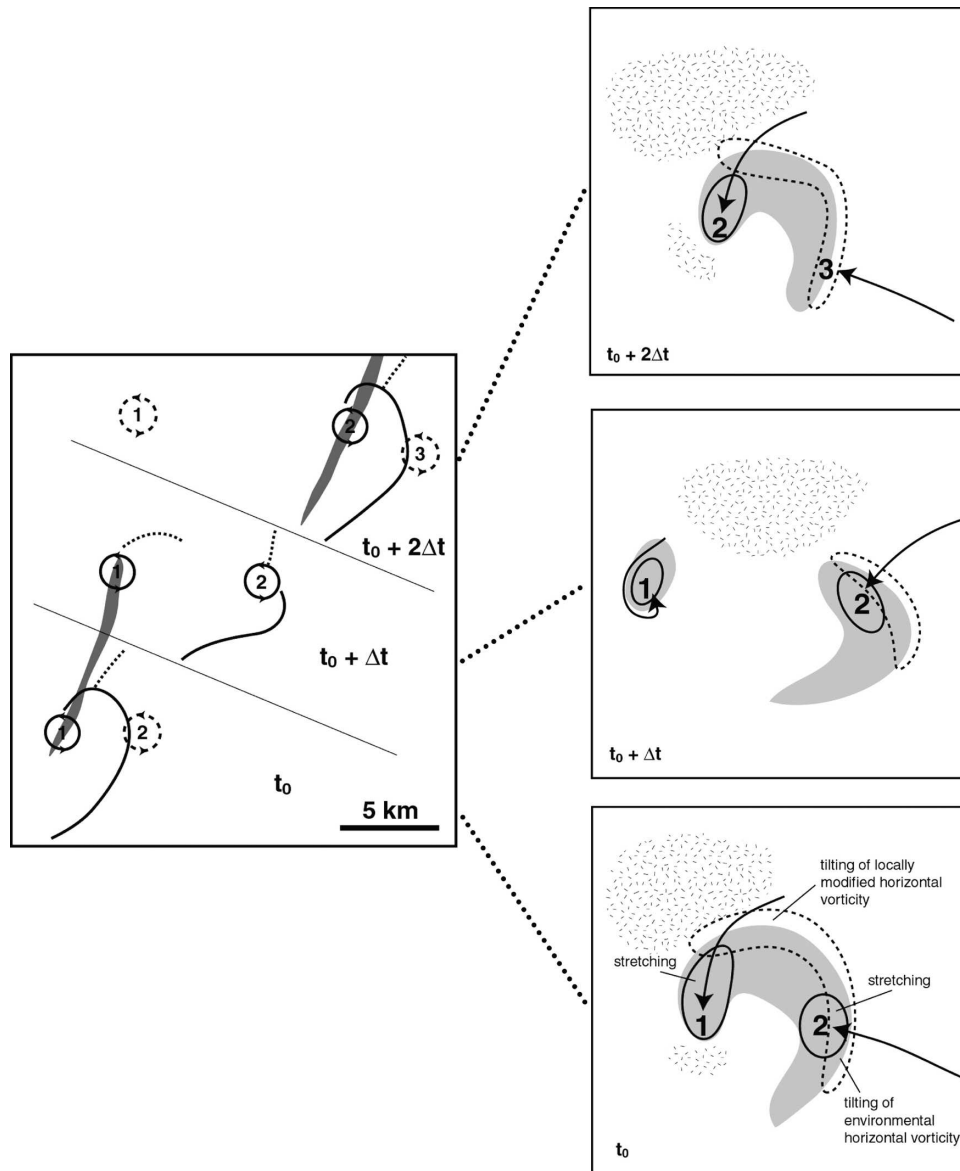


FIG. 2. Conceptual model of cyclic tornadogenesis from DB02b. Tornado tracks are shaded, while individual mesocyclones are numbered. Thin and dashed lines denote rear-flank and forward-flank wind shifts, respectively. Shading (speckling) indicates areas of updraft (downdraft) and arrows show vortex-relative trajectories. Dashed and solid outlines show regions of cyclonic vertical vorticity production via tilting of horizontal vorticity and stretching of vertical vorticity, respectively.

dataset of a cyclic supercell. The resolution of data within the low-level mesocyclones was on the order of 100 m across beam (from a distance of  $\sim 6$  km) and 37–74 m along beam for DOW3 and DOW2, respectively. The dataset supported an isotropic grid spacing of 100 m, dramatically reducing the three-dimensional size of resolvable features within the syntheses beyond that of previous studies. Additionally, the temporal spacing of the three-dimensional volume was finer than previously available. DOW-scanning strategies permit-

ted independent dual-Doppler syntheses every  $\sim 69$  s. In comparison, syntheses were conducted every  $\sim 360$  s for DB. Therefore, this dataset offered the possibility to evaluate cyclic dynamics and evolution on a temporal and spatial scale of exceptional quality.

The meteorological conditions surrounding the development of the Kress storm as well as the data collection techniques utilized are presented in section 2 of this study. The processing and synthesis methods are discussed in section 3. The bulk of the analysis can be

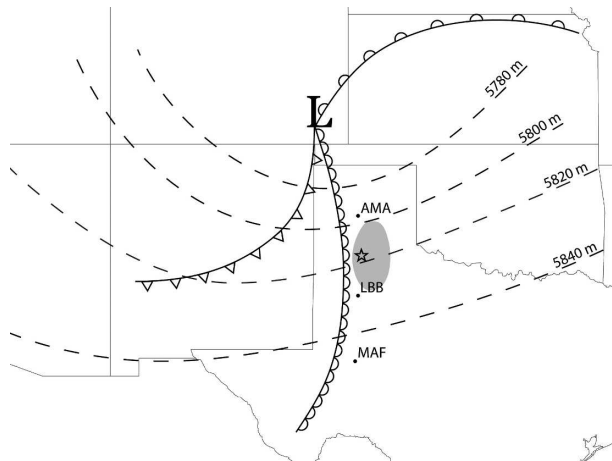


FIG. 3. Synoptic/mesoscale analysis valid during the dual-Doppler deployment time period compiled using 0000 UTC 30 May 2001 Eta model initialization data. The shaded area indicates CAPE values in excess of  $4000 \text{ J kg}^{-1}$ , while the star indicates the location of the dual-Doppler deployment near Kress, TX. The 500-mb height values are shown as dashed lines.

found within section 4, which provides insight into the structure and forcing mechanisms of prominent features found within the dataset. The main objective of this study, presented in section 5, was to assess similarities and differences between a high-resolution dataset of a cyclic supercell and past research, including previous conceptual models. An attempt to indicate potential mechanisms for the lack of tornadogenesis was also made in this section. Concluding remarks can be found in section 6.

## 2. The 29 May 2001 dataset

Throughout the afternoon and evening hours of 29 May 2001, a dryline and associated short wave were located in western Texas (Fig. 3). Ample support for supercell thunderstorms existed with upper-level divergence associated with the short wave, surface dryline convergence, and afternoon surface mixing ratios approaching  $22 \text{ g kg}^{-1}$  in the southern Texas Panhandle. In addition, both speed and directional wind shear aided in supercell development. Based on the 0000 UTC Eta model initialization for 30 May 2001, the region of interest east of the dryline contained surface winds of  $10 \text{ m s}^{-1}$  from the south-southeast with winds at 300 mb from the southwest at  $30 \text{ m s}^{-1}$ . The Eta model initialization also showed that the high moisture content in the southern panhandle was associated with late-day CAPE values of greater than  $4000 \text{ J kg}^{-1}$  (shaded region in Fig. 3) within the area of the DOW deployment.

The DOWs, participating in the Radar Observa-

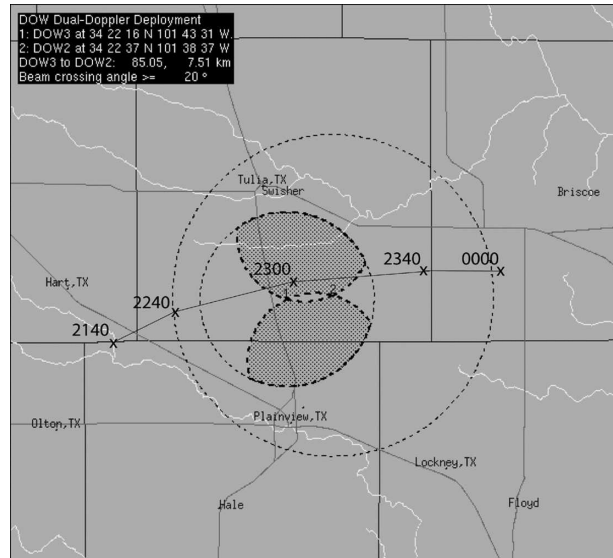


FIG. 4. Idealized schematic of the 29 May 2001 Kress, TX, DOW dual-Doppler deployment produced using the ViSky software package. DOW3 and DOW2 are located at positions "1" and "2," respectively. Thin dashed lines represent the azimuthal range used by both radars (14 km for DOW3 and 26 km for DOW2). Thick dashed lines demarcate the boundary of the dual-Doppler lobes given a beam-crossing angle of  $20^\circ$ . The hatched area inside each lobe represents areas where the beam-crossing angle is  $>20^\circ$ . Mesocyclone positions based on DOW data are plotted (times in UTC), showing movement of the storm before, during, and after the deployment. For scale, counties are about 50 km wide.

tions of Tornadoes and Thunderstorms Experiment (ROTATE), initially targeted a few weak cells that had developed along an outflow boundary just south of Amarillo, Texas. However, with these cells struggling to maintain strength in a premature environment, the DOWs eventually moved south as initiation associated with the dryline occurred in a broken line from just west of Amarillo to Plainview, Texas, around 2100 UTC. The DOWs eventually intercepted the southernmost of these cells around 2145 UTC near Kress.

A dual-Doppler deployment was conducted just east of Kress beginning at 2215 UTC and ending at 2310 UTC (Fig. 4). Both DOW2 and DOW3 radars transmitted a 3-cm wavelength beam and had a  $0.93^\circ$  beamwidth. Fast integration times allowed for oversampling of azimuths up to a factor of 3 and received signals were converted into radar moments such as reflectivity, radial velocity, spectral width, and signal-to-noise ratio. The scanning strategy adopted for this deployment consisted of sector volume scans of about  $150^\circ$  for DOW3 and about  $175^\circ$  for DOW2. The elevations used by DOW3 within the sector volume were  $0.5^\circ$ ,  $1.2^\circ$ ,  $2.0^\circ$ ,  $3.0^\circ$ ,  $4.0^\circ$ ,  $5.0^\circ$ ,  $6.0^\circ$ ,  $7.5^\circ$ ,  $9.0^\circ$ ,  $11.0^\circ$ ,  $13.0^\circ$ , and  $16.0^\circ$ . DOW2 scanned at identical elevations as DOW3 but

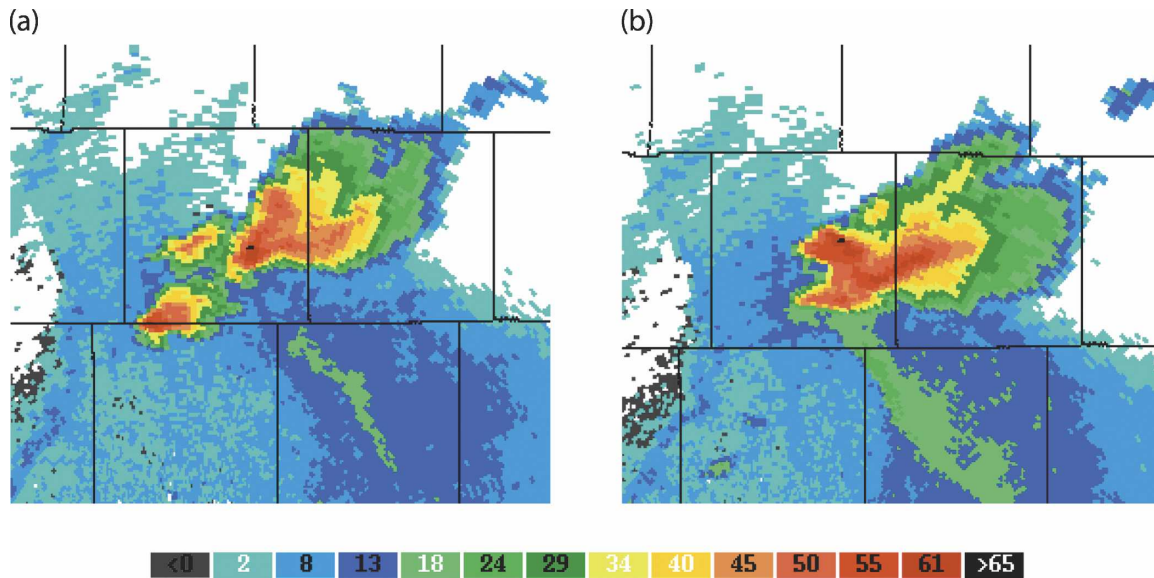


FIG. 5. The Lubbock, TX, Weather Service Radar  $0.5^\circ$  base reflectivity of the Kress storm and associated features. The storm was located approximately 85 km north of the radar. (a) At time 2304 UTC, two secondary cells are visible to the west and southwest of the main Kress storm. (b) Later at 2329 UTC, the right and left mover of the southwestern secondary cell have merged with the Kress cell, while the western secondary cell can be seen weakening to the north. Additionally, both the dryline and outflow boundary are visible.

included  $19.0^\circ$  and  $22.0^\circ$  as well. Gate spacing for DOW3 was 37 and 74 m for DOW2, while the azimuthal range for DOW3 was 14 and 26 km for DOW2.

The ViSky software package was used to produce the idealized dual-Doppler deployment schematic (Fig. 4). Illustrated are the dual-Doppler lobes (hatched) with heavy dashed lines indicating the boundaries of the lobes created with a  $20^\circ$  beam-crossing angle. Also shown with thin dashed lines are the azimuthal ranges of each radar. It should be noted that this schematic implies the usage of full plan position indicator (PPI) scans, not sector scans. Therefore, the dual-Doppler lobes shown should be considered an approximation of the actual dual-Doppler area for this deployment. The northern of these two lobes was chosen for data acquisition and the baseline of the deployment was 7.51 km. Mesocyclone positions are also plotted, indicating the path of the storm through the southern portion of the dual-Doppler lobe chosen for the deployment.

A combination of road network limitations and cell movement limited the vertical extent of the syntheses, specifically along the southern portion of the dataset. Within the region of the mesocyclones, the syntheses were limited to  $\sim 2$  km in height. This precluded the ability to analyze relationships between low-level and mid- to high-level dynamics within the mesocyclones. In addition, the close proximity of the storm to the baseline limited the time period of the syntheses due to an insufficiently small beam-crossing angle during the

beginning portion of the deployment. Therefore, data suitable for synthesis were limited to 2256–2310 UTC, representing 13 volumes of data, yet still providing an ample amount for analysis.

Significant evolution of the supercell and its mesocyclones occurred during the observation period. By the time of the dual-Doppler deployment, the supercell was well organized, having already developed a low-level mesocyclone. This mesocyclone had occluded by the start of the synthesis time period. Throughout the remainder of the deployment, two more mesocyclones formed, with evidence of a fourth mesocyclone forming during the last volume. In addition, although no tornadoes were produced during the deployment, eyewitness accounts, video shot by ROTATE crew, and the syntheses themselves show that low-level rotation was strong (vertical vorticity greater than  $10^{-2} \text{ s}^{-1}$ ) with each successive mesocyclone.

By 2304 UTC, during the latter portion of the deployment, several smaller cells had begun to develop just southwest of the main cell (Fig. 5a). The southern secondary cell split shortly after this time, with both the right- and left-moving elements eventually merging with the main supercell approximately 15 min after the end of the synthesis time period (Fig. 5b). Complex interactions and outflow from these secondary cells may have played a role in the low-level wind evolution toward the latter portion of the synthesis time period.

As the storm propagated eastward after the dual-

Doppler deployment, single-Doppler data from DOW3 shows that the storm continued to be cyclic in nature with three discrete mesocyclones present at 2340 UTC. By 2345 UTC, two mesocyclones are present, with the westernmost mesocyclone producing near-ground wind speeds of  $\sim 15 \text{ m s}^{-1}$ . At 2352 UTC, the storm contained one mesocyclone in addition to strong anticyclonic circulation aloft on the southern side of the hook echo, with winds of  $\sim 20 \text{ m s}^{-1}$  at  $13^\circ$  elevation. DOW3 navigator notes indicate both strong rear-flank downdraft (RFD) outflow and strong inflow associated with blowing dust at this time. Although no data exist during the first report of an observed tornado at 0010 UTC (3600 s after the end of the dual-Doppler deployment), single-Doppler data were collected on a tornado at 0108 UTC, containing winds of up to  $52 \text{ m s}^{-1}$ . While there were a number of other confirmed tornado reports, this tornado was the strongest observed with the storm.

Finally, the assessment of thermodynamic conditions during the deployment surrounding the Kress supercell was fairly difficult to make. The two closest observing stations, Plainview and the West Texas Mesonet station in Floydada, Texas (Schroeder et al. 2005), reported conditions that were not representative of the environment near the Kress supercell due to the passage of a predryline wind shift at 2200 UTC and an outflow boundary at 2230 UTC, respectively, well prior to the synthesis time period. In addition, the nearest upper-air sounding was from Amarillo at 1800 UTC, 5 h prior to the dual-Doppler deployment and about 90 km away. During 2001, the DOWs and support vehicles did not carry thermodynamic measurement instrumentation.

### 3. Processing and synthesis of data

#### a. Preprocessing

DOWs collect data in a raw personal computer (PC) Integrated Radar Acquisition II (PIRAQII) field format (Wurman 2001). Data are translated and parsed into perusable and editable sweep files using the SOLOII software suite (Oye et al. 1995). Data are subjectively edited to remove ground blockage, velocity and range folding, and other erroneous values. The Nyquist velocities were  $24 \text{ m s}^{-1}$  for DOW3 and  $21 \text{ m s}^{-1}$  for DOW2 during this deployment. With these values, velocity aliasing rarely exceeded one fold, making the unfolding process fairly straightforward. Narrow areas of partial blockage were a result of telephone poles lining the roads. Ground clutter was typically identified as having near-zero velocity and high returned power, enabling easy detection and removal.

Individual sweep files also required an orientation correction to navigate the data precisely to earth-

relative coordinates. Using the telephone poles as a proxy for the location of roads, it was possible to align clutter targets in sweep files on a road grid. This process was conducted for both DOW2 and DOW3 sweep files. Another unique processing requirement of DOW data prior to 2002 is "dejittering." In 2001, lags in the tagging of angles by the signal processing systems and gear backlash in the antennas caused small errors in the recording of azimuth angles that varied depending on whether scans were proceeding clockwise or counterclockwise. The net effect is a clockwise and counterclockwise jittering or shifting of successive sweeps. The magnitude of the effect is small (tenths of degrees) but was removed to increase the precision of the navigation of the data.

The usual method used to correct this error involves the identification of a prominent steady-state phenomenon, such as a tornado, that exists throughout a volume. The azimuthal position of this object can be plotted versus height within one volume. Linear regression can then be used to approximate the location of the object without any jittering. Then each sweep can be corrected based on the azimuthal distance of the object from the regression line (Alexander and Wurman 2005).

Unfortunately, the 29 May 2001 dataset lacked any steady-state phenomena, due to the nontornadic nature of the storm during the synthesis time period and the rapidity of the cycling that occurred. Based on experience from other similar deployments, this problem was rectified by alternately rotating successive sweeps by  $\pm 0.3^\circ$ , adjacent sweeps positively (clockwise) and negatively (counterclockwise).

#### b. Interpolation

After editing, the National Center for Atmospheric Research's (NCAR's) REORDER (Oye et al. 1995) was used to interpolate data onto a Cartesian grid. The Barnes weighting scheme was chosen for the interpolation (Barnes 1964; Koch et al. 1983) and an isotropic grid spacing of 100 m was used, given that both along- and cross-beam resolutions within the primary area of interest were below this value. However, since derived fields involving derivatives such as divergence and vorticity are sensitive to noise and can be very difficult to analyze when synthetic artifacts are included, two objective analyses were conducted for each volume.

The first objective analysis was solely for the analysis of the wind field, while the second analysis was designed to produce relatively smooth derived fields. An isotropic radius of influence of 400 m was used for the first objective analysis. Given this type of interpolation, a theoretical response of 50% for the Barnes filter occurred at a wavelength of 0.675 km (5% at 0.325 km).

Grid spacing for the second analysis was the same, but a slightly larger radius of influence (0.5 km) was used in order to obtain a smoother wind field. The second objective analysis resulted in a theoretical response of 50% for the Barnes filter at a wavelength of 0.847 km (5% at 0.406 km).

Based on Carbone et al. (1985), at least six grid points are necessary to resolve a specific feature or phenomenon. For the primary interpolation of the 29 May 2001 dataset, this would be 600 m. Compared with 2800 m for the McLean syntheses of DB, the current volumetric resolution is  $\sim 100$  times finer. Additionally, temporal sampling in the current analysis is 5 times faster than DB, resulting in 500 times finer 4D resolution.

### c. Synthesis

The NCAR Custom Editing and Display of Reduced Information in Cartesian Space (CEDRIC) software package (Miller and Fredrick 1998) was used to synthesize the data. Prior to synthesis, vertical velocity contamination was removed from the horizontal velocity components. CEDRIC uses a reflectivity–fall speed relationship based on dBZ values of reflectivity to correct for this error. After horizontal synthesis, calculation of vertical velocity requires the use of the mass continuity equation, which was integrated upward from the ground, with a surface boundary condition of  $w = 0$ . Prior to the calculation of derived fields, a one-step, two-dimensional Leise filter (Leise 1982) was applied to both the velocity and reflectivity data at each level. Finally, derived quantities, including vorticity, divergence, certain terms of the vertical vorticity tendency equation, and resultant deformation, were calculated using the syntheses of the secondary objective analyses.

### d. Vertical vorticity tendency and deformation equation calculation

The calculation of both vertical vorticity tendency and deformation terms involved the discretization of differential equations in CEDRIC. Calculation of vertical vorticity tendency terms was completed using a simplified version of the vertical vorticity tendency equation [Eq. (2.1) in DB02b]. Solenoidal production of vertical vorticity was neglected due to scale analysis (Heysfield 1978) and frictional production was neglected due to observational limitations. Following these simplifications, the equation becomes

$$\frac{\partial \zeta}{\partial t} = - \left( u \frac{\partial \zeta}{\partial x} + v \frac{\partial \zeta}{\partial y} \right) - w \frac{\partial \zeta}{\partial z} + \left( \frac{\partial u}{\partial z} \frac{\partial w}{\partial y} - \frac{\partial v}{\partial z} \frac{\partial w}{\partial x} \right) - \delta \zeta, \quad (1)$$

where  $\zeta$  is vertical vorticity and  $\delta$  is horizontal divergence. The terms on the right represent advection, tilting, and stretching of vorticity.

Total deformation is the combination of the shear and stretching components as follows:

$$|D| = \sqrt{\left( \frac{\partial u}{\partial x} - \frac{\partial v}{\partial y} \right)^2 + \left( \frac{\partial v}{\partial x} + \frac{\partial u}{\partial y} \right)^2}. \quad (2)$$

This represents the scalar magnitude of the resultant deformation. The deformation components are not rotationally invariant by themselves. However, the sum of the squares of the components is invariant, allowing deformation tick marks to be plotted based on a standard Cartesian grid. These tick marks are bidirectional in nature and have an alignment parallel to the axis of dilatation. They are also proportional in length to the magnitude of the resultant deformation.

Deformation analysis has been conducted on larger, synoptic-scale phenomena in the past (Bluestein 1977). However, application to smaller convective features, including supercells, has not been widely conducted. The impinging inflow and outflow pattern associated with low-level supercell thunderstorm flow qualitatively appears to represent an area of deformation, possibly contributing to the development and evolution of the hook echo. This hypothesis contends that an axis of dilatation is oriented parallel to the hook echo, while an axis of contraction lies parallel to the inflow/outflow. The Kress storm provided an excellent opportunity to assess this possibility.

## 4. Analysis and results

### a. General supercell and mesocyclone vertical structure

Prior to the presentation of results, it is informative to discuss the classic definition of a mesocyclone and to consider its application in the context of this paper. It has been traditionally accepted that a circulation must meet criteria related to diameter and vertical vorticity in order to be classified as a mesocyclone. A diameter of 2–10 km and a minimum vertical vorticity of  $10^{-2} \text{ s}^{-1}$  are generally considered to be sufficient (Huschke 1959). Within the context of this paper, the traditional definition of a mesocyclone holds, with the minor exception of the minimum diameter criterion, which has been changed from 2 to 1 km. This alteration can be permitted in this case because low-level mesocyclones are being considered and are generally smaller than midlevel mesocyclones. Therefore, all mesocyclones described hereafter are at least 1 km in diameter and are defined based on the area bounded by vertical vorticity of  $10^{-2} \text{ s}^{-1}$ . Finally, although a vertical depth cri-

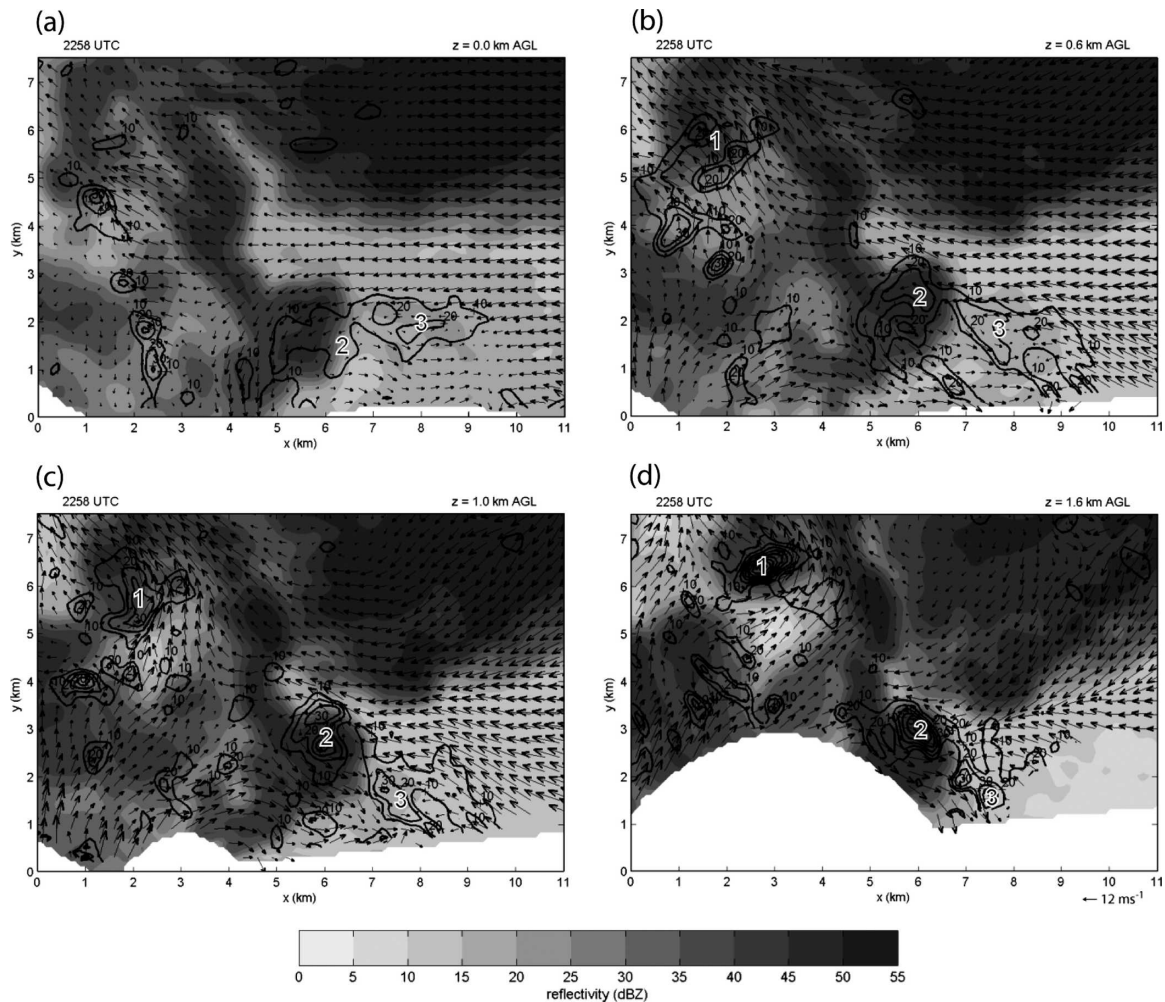


FIG. 6. Horizontal cross sections of reflectivity, storm-relative horizontal wind vectors, and contours of positive vertical vorticity (intervals of  $10 \times 10^{-3} \text{ s}^{-1}$ ) from the 2258 UTC volume: (a) 0.0, (b) 0.6, (c) 1.0, and (d) 1.6 km AGL. Wind vector length equal to one grid spacing is  $4 \text{ m s}^{-1}$  (every third grid point is shown). Mesocyclones are numbered.

terion is sometimes included in the definition of a mesocyclone, it is not considered in this case, owing to the limited depth of the vertical domain.

Although the Kress supercell was undergoing major dynamical evolution throughout the synthesis time period, a number of vertically consistent features persist throughout all 12 volumes, but contain specific characteristics that vary with height. A representative volume (2258 UTC) has been chosen in order to discuss and compare these features and their characteristics to previous research. Horizontal cross sections have been created from the 2258 UTC volume at heights of  $z = 0.0$ ,  $0.6$ ,  $1.0$ , and  $1.6 \text{ km AGL}$  (Fig. 6).

The surface wind field shows a broad region of vorticity encompassing the two surface mesocyclones (Fig. 6a). Relatively weak vorticity (barely reaching mesocyclone criteria) was associated with mesocyclone 2, while

mesocyclone 3 contains vorticity up to  $20 \times 10^{-3} \text{ s}^{-1}$ . Cyclonic flow associated with the first reflectivity hook echo ( $x = 2$ ,  $y = 5.5$  in Fig. 6a). However, pockets of vertical vorticity (which exceed the strength of surface vorticity associated with the mesocyclones) existed along a linear surface convergence feature that extends from just south of the initial mesocyclone ( $x = 1$ ,  $y = 4.5$ ) to west of the mature hook echo ( $x = 2.5$ ,  $y = 1$ ).

Associated with surface mesocyclones 2 and 3 was a rear-flank gust front extending out to the east and then south with dBZ values of about 25. Propagating well ahead of the hook echo, the rear-flank gust front was the only surface boundary associated with the surface mesocyclones. There was a lack of a distinct forward-flank gust front in the wind field at the surface. Easterly flow can be seen both within the precipitation-free in-

flow and precipitation-filled forward-flank regions with no convergence apparent along the forward-flank reflectivity gradient. Recent research, including Dowell and Bluestein (1997) and DB02a, has shown that both the existence and orientation of the low-level forward-flank gust front (as seen in the conceptual model of Burgess et al. 1982) are ambiguous for some storms.

At 600 m AGL (Fig. 6b), both mesocyclones 2 and 3 became much better defined and structured with regard to both the wind and vorticity fields (vorticity values up to  $20 \times 10^{-3} \text{ s}^{-1}$ ). Mesocyclone 2 was completely within the precipitation-filled hook echo at this height and was located significantly farther north than at the surface (vertical continuity of mesocyclone 2 between the surface and 600 m was verified using intermediate levels of the synthesis). In contrast, mesocyclone 3 still remained in the same location within the precipitation-free updraft. This result may suggest that mesocyclone 2 was experiencing differential advection of vorticity, while the newer mesocyclone 3 was able to maintain vertical continuity. Mesocyclone 1 was now apparent with vertical vorticity values around  $10\text{--}20 \times 10^{-3} \text{ s}^{-1}$ , in addition to a slight amount of cyclonic curvature in the wind field. There was still no definite indication of any forward-flank gust front. In addition, the distance between the hook echo and the forward-flank precipitation had decreased. In other words, the hook echo tilted toward the northeast with height while the forward-flank precipitation tilted toward the south, indicating a precipitation overhang or weak-echo region (WER).

At 1.0 km AGL (Fig. 6c), the locations of all three mesocyclones had remained relatively unchanged, with the exception of only slight movement for mesocyclones 2 and 3. The vorticity associated with each mesocyclone was stronger at this height, with maximums of  $30 \times 10^{-3} \text{ s}^{-1}$ ,  $40 \times 10^{-3} \text{ s}^{-1}$ , and  $30 \times 10^{-3} \text{ s}^{-1}$  for mesocyclones 1, 2, and 3, respectively. The vorticity centers had also become more compact and concentrated, collocated with the centers of circulation in the wind field. In addition, it was at this level that the first signs of general convergence associated with the forward-flank reflectivity gradient were evident.

By 1.6 km AGL (Fig. 6d), the vertical limit of the synthesis domain within the area of interest was close to being reached. However, it was at this height that a dramatic increase in vorticity existed. The vertical vorticity of mesocyclone 1 was approaching  $10^{-1} \text{ s}^{-1}$ , with the wind field exhibiting strong cyclonic curvature associated with the receding initial hook echo. Mesocyclone 2, with vertical vorticity of  $60 \times 10^{-3} \text{ s}^{-1}$ , was significantly stronger than at all levels below. The position of mesocyclones 2 and 3 remained relatively unchanged with height at this level; however, mesocyclone

1 was about 0.5–1.0 km farther north than at 1.0 km AGL. Finally, another primary feature of interest at this level was the forward-flank gust front. Showing a remarkably linear nature, it was dramatically stronger and more concentrated than at the previous level of 1.0 km AGL (Fig. 6c).

These features persisted throughout the other independently calculated synthesis volumes. Newly formed mesocyclones appeared vertically stacked with height; while mature to occluded mesocyclones had a prominent shear-induced tilt to their vertical structure. Furthermore, vertical vorticity increased with height within occluded mesocyclones, whereas it appeared to be vertically consistent within newly developed mesocyclones. Finally, mesocyclogenesis occurred along the precipitation-free rear-flank gust front in absence of any forward-flank boundary.

#### b. General supercell and mesocyclone evolution

The assessment of the cyclic and overall evolution of the Kress storm was conducted at an estimated cloud-base level of  $\sim 1.0$  km AGL. This lifting condensation level (LCL) was estimated using data from two West Texas Mesonet observing stations located in Floydada and Plainview, as mentioned previously. Because of the aforementioned uncertainty in the thermodynamic data from these two stations, an average temperature and dewpoint were computed. Cross sections at 1.0 km AGL from the synthesis of each volume (about every minute) can be seen in Figs. 7 and 8.

At the beginning of the synthesis time period, three distinct mesocyclones were visible. The occlusion of mesocyclone 1 had occurred prior to the deployment and along with the initial hook echo, it had begun to deviate toward the northwest relative to storm motion. Vertical vorticity associated with mesocyclone 1 at this time was around  $20\text{--}30 \times 10^{-3} \text{ s}^{-1}$  (Fig. 8a). At 2256 UTC, mesocyclone 2 existed within the vertical velocity gradient associated with the updraft within the inflow and the downdraft of the hook echo (Fig. 7a). A well-organized area of vorticity (up to  $30 \times 10^{-3} \text{ s}^{-1}$ ) was associated with mesocyclone 2 at this time (Fig. 8a). In addition, the third and newest mesocyclone had formed quite recently, completely within the updraft, embedded within vertical motion of  $\sim 7 \text{ m s}^{-1}$  and vertical vorticity of up to  $20 \times 10^{-3} \text{ s}^{-1}$  (Figs. 7a and 8a). Formation of the newest mesocyclone occurred along the rear-flank gust front in absence of any forward-flank gust front with an initial diameter of about 0.5 km. At 1.0 km AGL, there was a signal of a forward-flank convergence zone just south of the reflectivity gradient; however, due to the large separation between the newly formed hook echo and the forward flank, this conver-

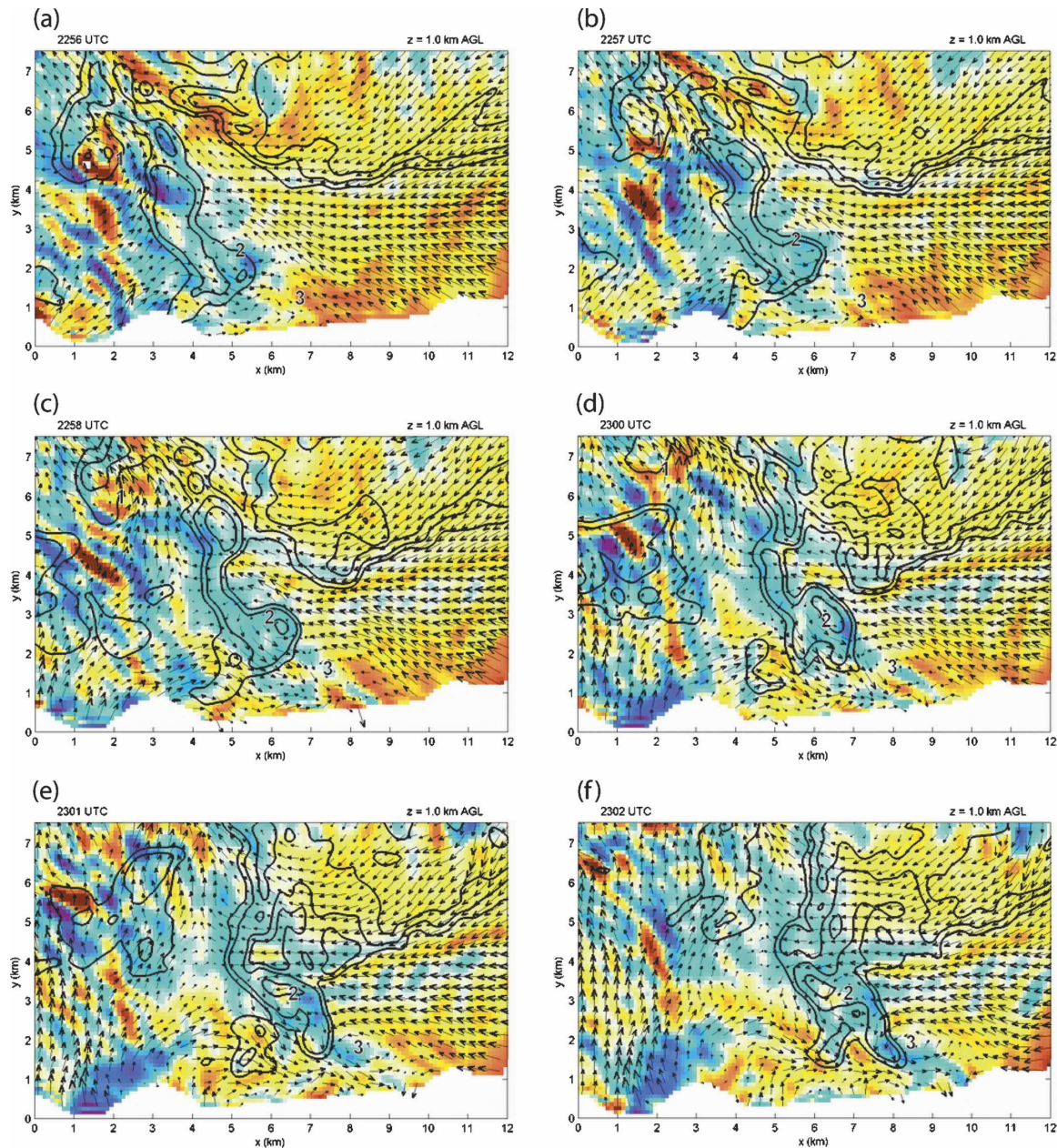


FIG. 7. Horizontal cross sections of contoured reflectivity (40, 45, and 50 dBZ), storm-relative horizontal wind vectors, and vertical velocity at 1.0 km AGL from each synthesis volume: (a) 2256, (b) 2257, (c) 2258, (d) 2300, (e) 2301, (f) 2302, (g) 2303, (h) 2304, (i) 2306, (j) 2307, (k) 2308, and (l) 2310 UTC. Wind vector length equal to one grid spacing is  $4 \text{ m s}^{-1}$  (every third grid point is shown). Mesocyclones are numbered.

gence zone was not associated with the development of mesocyclone 3.

By 2258 UTC, mesocyclone 1 continued to move farther north relative to storm motion but had maintained vertical vorticity of  $30 \times 10^{-3} \text{ s}^{-1}$  (Figs. 7c and 8c). Also at this point, mesocyclone 2 was being overtaken by its associated hook echo, resulting in a dominance of negative vertical velocity within the mesocyclone. However,

vertical vorticity associated with mesocyclone 2 increased to  $30\text{--}40 \times 10^{-3} \text{ s}^{-1}$  (Fig. 8c). Mesocyclone 3 continued to mature at 2258 UTC, with a diameter of about 1.0 km (Figs. 7c and 8c).

The distance between the forward flank and the main hook echo had decreased between 2256 and 2258 UTC as occlusion of the second mesocyclone coincided with the movement of its associated hook echo toward the

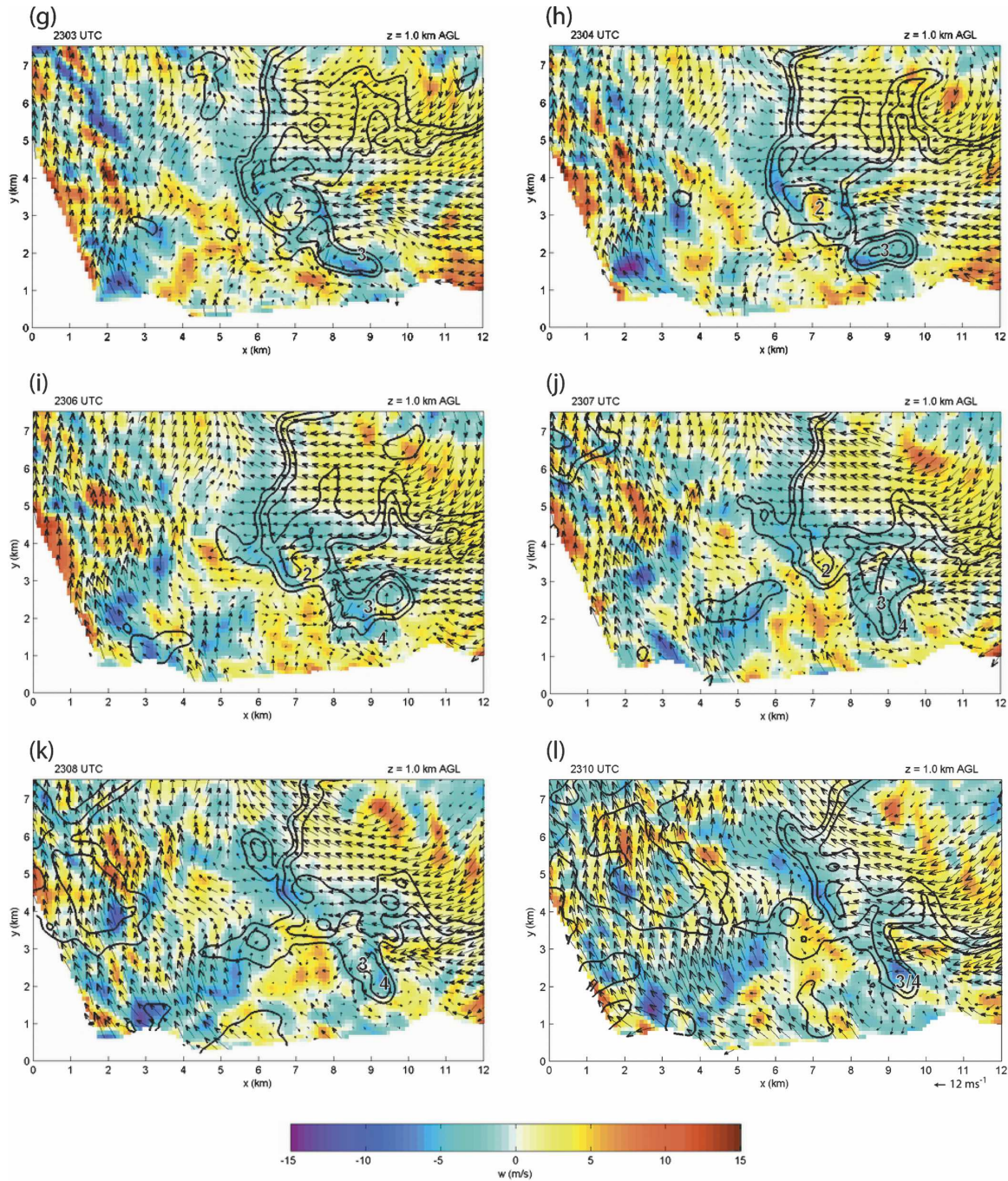


FIG. 7. (Continued)

north. After this occlusion, a new reflectivity tendril associated with the next hook echo can be seen by 2300 UTC on the southeastern edge of hook echo 2 (Figs. 7d and 8d). This new area of precipitation became the new hook echo by 2301 UTC as hook echo 2 began to merge with the forward flank. By 2302 UTC, the new hook echo had begun to wrap cyclonically around mesocyclone 3, which had reached a diameter of about 2 km

(Figs. 7f and 8f). The described hook echo evolution for the second mesocyclone is similar to that of the first mesocyclone, where the associated hook echo migrated toward the forward flank while a new tendril in reflectivity began to develop toward the southeast. This evolution occurred prior to the synthesis time period and was documented using single-Doppler data.

While there was no evidence of mesocyclone 1 or the

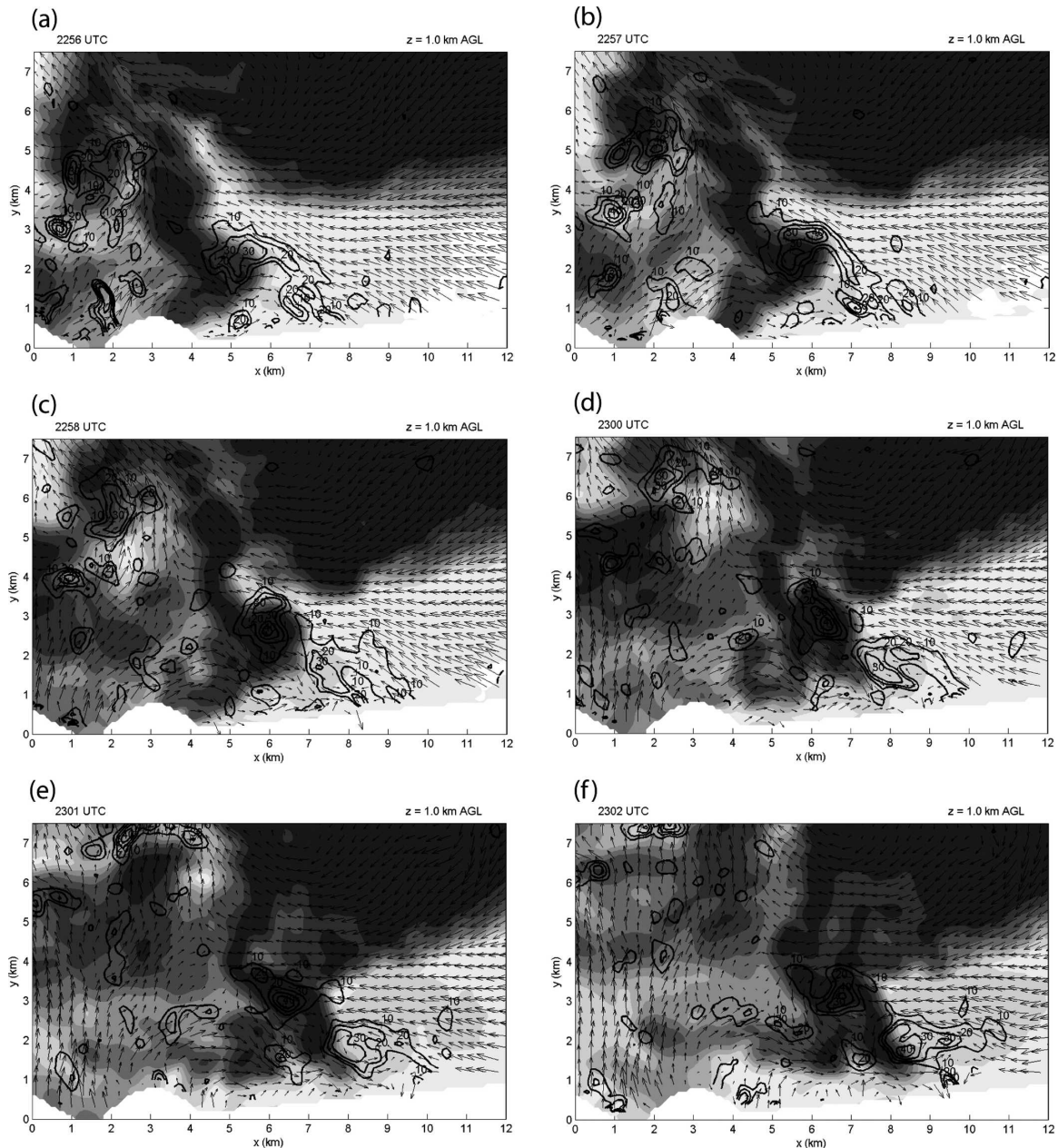


FIG. 8. Same as in Fig. 7, but for reflectivity, storm-relative horizontal wind vectors, and positive vertical vorticity (intervals of  $10 \times 10^{-3} \text{ s}^{-1}$ ) at 1.0 km AGL from each synthesis volume.

initial hook echo by 2301 UTC, mesocyclone 2 sustained its intensity at 2302 UTC with vertical vorticity of up to  $40 \times 10^{-3} \text{ s}^{-1}$  (Fig. 8f). Mesocyclone 3 continued to increase in strength, containing a maximum in vertical vorticity of  $40 \times 10^{-3} \text{ s}^{-1}$  (Fig. 8f). It is also at this time that there was noticeable southerly flow beginning to replace westerly flow along the extreme southern periphery of the domain ( $x = 4$  to  $x = 7.5$  in Figs. 7f and 8f). This southerly flow increased in subsequent syntheses, marking the arrival of outflow asso-

ciated with separate cells developing to the south and west.

By 2303 UTC, mesocyclone 3 had become half enveloped by the newly developed hook echo and was fully immersed in precipitation by 2304 UTC (Figs. 7g,h and 8g,h). With the occlusion of mesocyclone 3, the hook echo had begun to migrate toward the north, as the second hook echo did with mesocyclone 2 (Figs. 7h and 8h). This evolution would naturally lead to the development of the next mesocyclone. Signs of a new

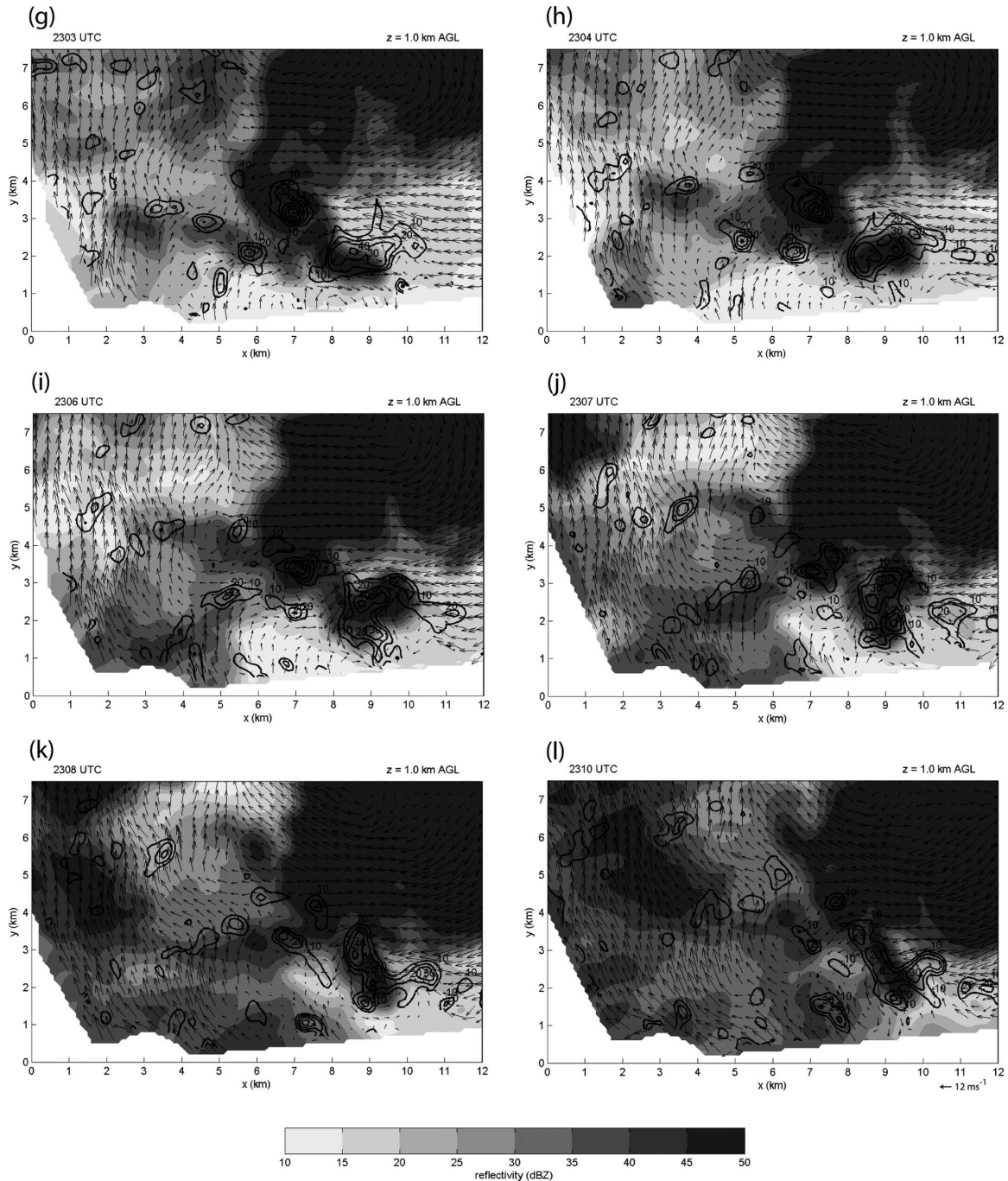


FIG. 8. (Continued)

circulation can be seen by 2306 UTC ( $x = 9, y = 1.5$  in Figs. 7i and 8i). However, this new circulation never completely developed into a mesocyclone. Instead, the new vorticity maximum, mesocyclone 3, and a vorticity maximum that developed within the inflow near the stalled RFD boundary at 2306 UTC ( $x = 11, y = 2$  in Figs. 7i and 8i) began to rotate about a central location in the wind field ( $x = 9.5, y = 2$  in Fig. 7l). Even though

a new hook echo was created by 2308 UTC, it did not appear to be associated with one specific vorticity maximum or mesocyclone (Figs. 7k,l and 8k,l).

Toward the end of the synthesis time period, the forward progression of the storm at 1.0 km AGL had decreased markedly. It is possible that this was due to the intrusion of southerly flow west and south of the storm, which by 2307 UTC had completely replaced a majority

of the westerly momentum previously in place ( $x = 3$  to  $x = 8.5$  in Figs. 7j and 8j). Another possibility is that the rear-flank downdraft had weakened, reducing the amount of westerly flow needed for rapid eastward progression of the RFD boundary. Regardless of the cause, the reduction of westerly momentum in the rear flank was likely a reason for the incomplete cycle that precluded the development of mesocyclone 4.

The distance between the hook echo and the forward flank had decreased remarkably from the beginning to end of the synthesis time period. DOW observations and video of the storm just prior to the beginning of the dual-Doppler deployment showed that the storm had a “low precipitation” to “classic” structure. However, the storm appeared to have begun a transition to “high precipitation” (HP) during the deployment, as a decreasing WER was accompanied by increasing precipitation in the rear flank of the storm shortly after the end of the deployment. The HP nature of the storm is visible in video and radar observations later during the day.

As with the vertical structure, there are evolutionary characteristics that are repeated throughout the synthesis time period. Primarily, it was found that mesocyclones formed in regions that contained only updraft and matured in regions containing vertical velocity gradients split between both updraft and downdraft air. Occluded mesocyclones were generally dominated by negative vertical velocity associated with the collocation with precipitation-filled hook echoes (well after occlusion, pockets of positive vertical velocity reappeared, such as in mesocyclones 1 and 2). In addition, vertical vorticity values within occluded mesocyclones 2 and 3 showed that decay was not an immediate process, even with the prevalence of negative vertical velocity. Finally, hook echo evolution and motion was observed to be closely related to the evolution of the mesocyclones, with each hook echo migrating toward the forward flank and occluding along with the associated mesocyclone.

### c. Cycling frequency calculation

Given the observed rapidity of both occlusion and hook echo evolution, an attempt was made to quantify the cycling frequency of the storm during the synthesis time period. To determine the frequency, a methodology similar to that used by Burgess et al. (1982) was adopted, with the amount of time elapsed between mature stages of each mesocyclone delineating one cycle. A mature mesocyclone was defined in terms of its position relative to the vertical velocity gradient associated with the reflectivity hook echo (Lemon and Doswell 1979). The mature stage was reached once the hook echo had eclipsed half of the mesocyclone, result-

ing in an equally split vertical velocity profile within the mesocyclone.

At the onset of the synthesis (2256 UTC), the first mesocyclone had occluded, while mesocyclone 2, being half within updraft and half within downdraft, was currently mature. Therefore, the second and third mesocyclones were included in the cyclic frequency formation. While the partially developed fourth mesocyclone did not contain a closed circulation in the wind field, it contained vertical vorticity values sufficient for mesocyclone criteria (up to  $40 \times 10^{-3} \text{ s}^{-1}$ ) and a split vertical velocity profile necessary to be declared mature. Based on these findings, the cycle from mesocyclone 3 to partial mesocyclone 4 was found to be acceptable for use in the cycling frequency calculation as well. An inherent assumption of this calculation is that the second mesocyclone had reached maturity at 2256 UTC, marking the beginning of the deployment. This assumption is deemed to be fairly accurate, given the position of the mesocyclone relative to the hook echo at this time, and given that the time spent in the mature stage for the latter mesocyclones was on the order of 1 to 2 min.

Between 2302 and 2303 UTC, the third mesocyclone reached maturity. The partial fourth mesocyclone reached “occlusion” around 2307 to 2308 UTC, quickly after its formation. Therefore, 6–7 min elapsed between the maturity of mesocyclones 2 and 3, and about 5 min elapsed between the maturity of mesocyclone 3 and partial mesocyclone 4. This result is averaged for a general cycling frequency of about 6 min during the synthesis time period.

### d. Low-level mesocyclone analysis

A number of previous studies have analyzed the structure and vorticity budget of supercell low-level flow in order to better understand the origins of vorticity associated with mesocyclones and tornadoes. Ideally, for tornadic vorticity origins, these fields should be analyzed as close to the surface as possible in order to resolve near-ground wind field characteristics (Rotunno and Klemp 1985; Wicker and Wilhelmson 1995). Previous observational studies have been limited in their ability to resolve wind characteristics close to the ground. An advantage of using ground-based radar is the ability to analyze fields near the surface. In this case, vertical vorticity tendency was analyzed at 200 m AGL.

Figure 9 shows the representative low-level wind structure of the Kress storm at the time of the analysis. The image is from the 2256 UTC volume, and the wind field with associated rear-flank gust front is associated with mesocyclones 2 and 3. In addition to wind vectors

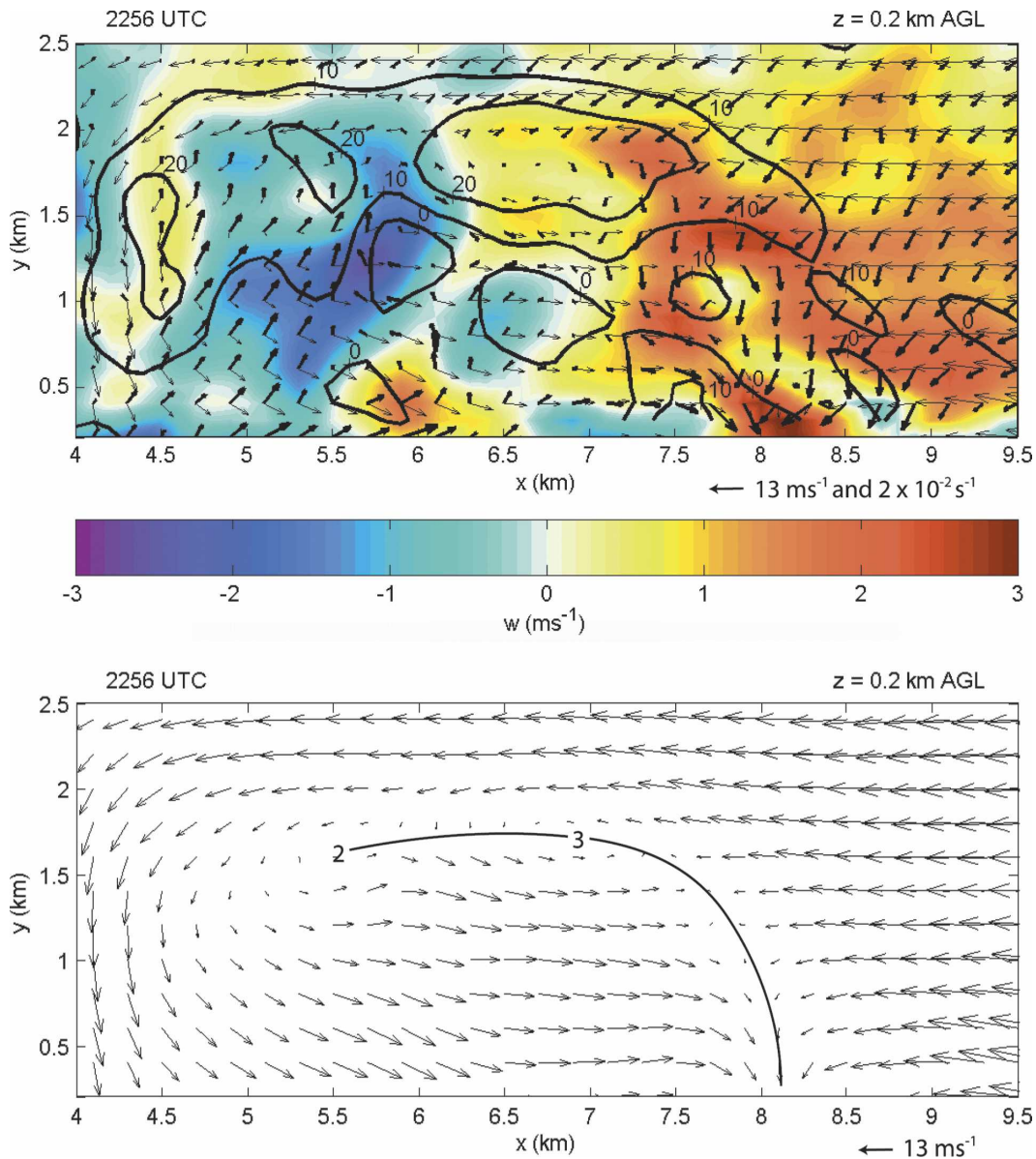


FIG. 9. Representative horizontal cross section of storm-relative wind vectors, horizontal vorticity vectors (bold-face), and vertical vorticity contours (intervals of  $10 \times 10^{-3} \text{ s}^{-1}$ ) within the vicinity of the low-level mesocyclones at 200 m AGL. Wind vector length equal to grid spacing is  $6.5 \text{ m s}^{-1}$  (every other grid point is shown). Horizontal vorticity vector length equal to grid spacing is  $10^{-2} \text{ s}^{-1}$ . Mesocyclones are numbered and the thick line represents the position of the rear-flank gust front.

and vertical vorticity contours, low-level horizontal vorticity vectors (in bold) have been overlaid. This perspective allows one to understand the orientation of horizontal vorticity relative to the wind (i.e., crosswise or streamwise horizontal vorticity). Analysis of the low-level horizontal vorticity field indicates that a large component of crosswise vorticity existed throughout the low-level mesocyclones, both in the updraft and downdraft regions. Comparison of multiple levels of the 2256 UTC synthesis showed that the vertical profile

of the wind within the lowest 800 m of the storm contained little directional turning with height. This uniformity resulted in the predominantly crosswise horizontal vorticity.

Previous research has shown that tilting of streamwise vorticity is not only more favorable for midlevel rotation, but within the lower levels of the storm, it is more conducive to tornadic development than crosswise vorticity (Davies-Jones 1984; Rotunno and Klemp 1985; Davies-Jones and Brooks 1993). Observational

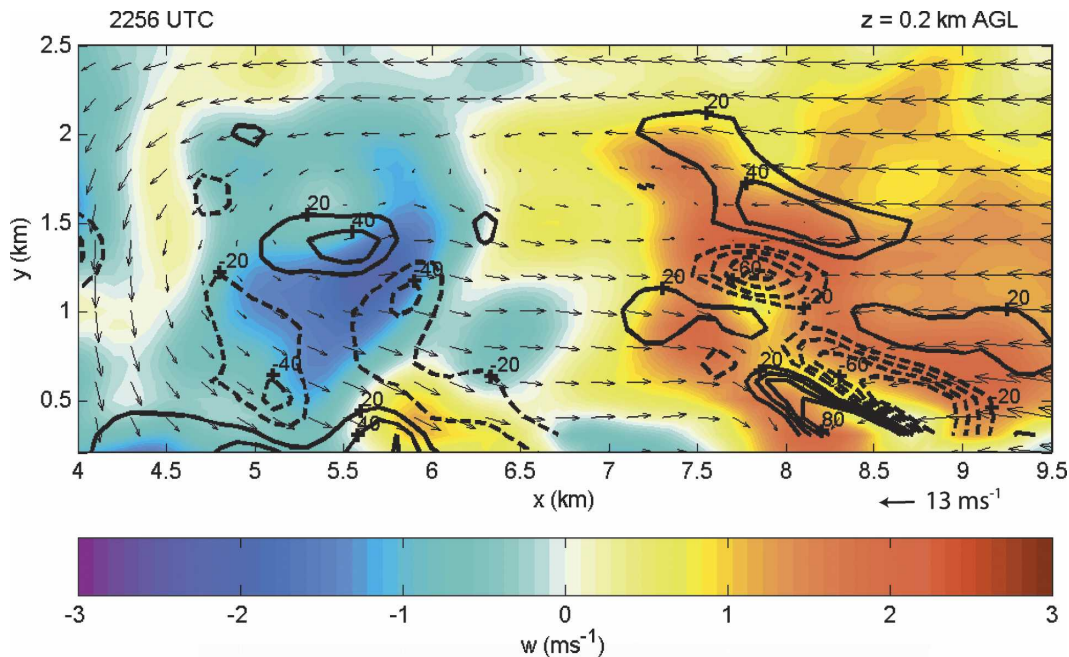


FIG. 10. Plot of storm-relative wind vectors ( $\text{m s}^{-1}$ ) and contours of tilting (intervals of  $20 \times 10^{-6} \text{ s}^{-2}$ ) within the vicinity of the low-level mesocyclones. Solid tilting contours indicate positive vertical vorticity tilting, while dashed tilting contours indicate negative vertical vorticity tilting. Wind vector length equal to grid spacing is  $6.5 \text{ m s}^{-1}$  (every other grid point is shown).

evidence exists to confirm this theory both in the Del City/Fort Cobb, Oklahoma, storms of Johnson et al. (1987) and the McLean storm of DB, where streamwise vorticity existed within low-level inflow regions of the storms and tornadogenesis resulted shortly thereafter.

Tilting of crosswise versus streamwise vorticity produces very different outcomes in terms of the resultant vertical vorticity field. Davies-Jones and Brooks (1993) asserted that tornadogenesis may be the result of tilting of both baroclinic and barotropic streamwise vorticity within the downdraft region of the mesocyclone. When both baroclinic and barotropic effects on tilting within the downdraft are incorporated, a single region of cyclonic vertical vorticity is produced. They showed that tilting of purely crosswise vorticity within the downdraft is not conducive to the development of tornadic-scale low-level vorticity. Instead, this process produces a vortex couplet with each vortex displaced on either side of the center of the downdraft (Fig. 9 of Davies-Jones and Brooks 1993).

A plot of the tilting term within the area of the low-level mesocyclones is shown in Fig. 10. Tilting within the downdraft region is almost identical to the crosswise horizontal vorticity example within Fig. 9 of Davies-Jones and Brooks (1993). Because the vorticity is crosswise, tilting creates a vertical vorticity couplet, with cyclonic tilting to the left (following the flow), and anticyclonic tilting to the right. When air is tilted within

the inflow of the Kress storm, the same scenario exists, but in opposite locations from that in the downdraft region.

Subsequent stretching of tilted vertical vorticity is largely dependent upon the type of horizontal vorticity present. A plot of the stretching term is shown in Fig. 11 and shows, as expected, that the strongest stretching is located near areas with the strongest values of vertical motion and vorticity. However, because the low-level horizontal vorticity is mostly crosswise, the maxima in vertical motion and vertical vorticity are not collocated. Therefore, stretching of vertical vorticity is not maximized in this case and would have been much stronger had a larger streamwise horizontal vorticity component been present. This result may well have limited the strength of the low-level circulations within the Kress storm.

Some observational studies, including Brandes (1984, 1993) and Johnson et al. (1987), showed evidence that, given streamwise vorticity within the inflow, tornadogenesis is possible concurrent with crosswise vorticity behind the rear-flank gust front. And while streamwise vorticity existed throughout the low levels of the McLean storm, DB attributed tornadogenesis within the McLean storm to inflow streamwise vorticity tilting and stretching, showing no evidence of strong vorticity tilting within the downdraft region.

The difference between the Kress storm and that of

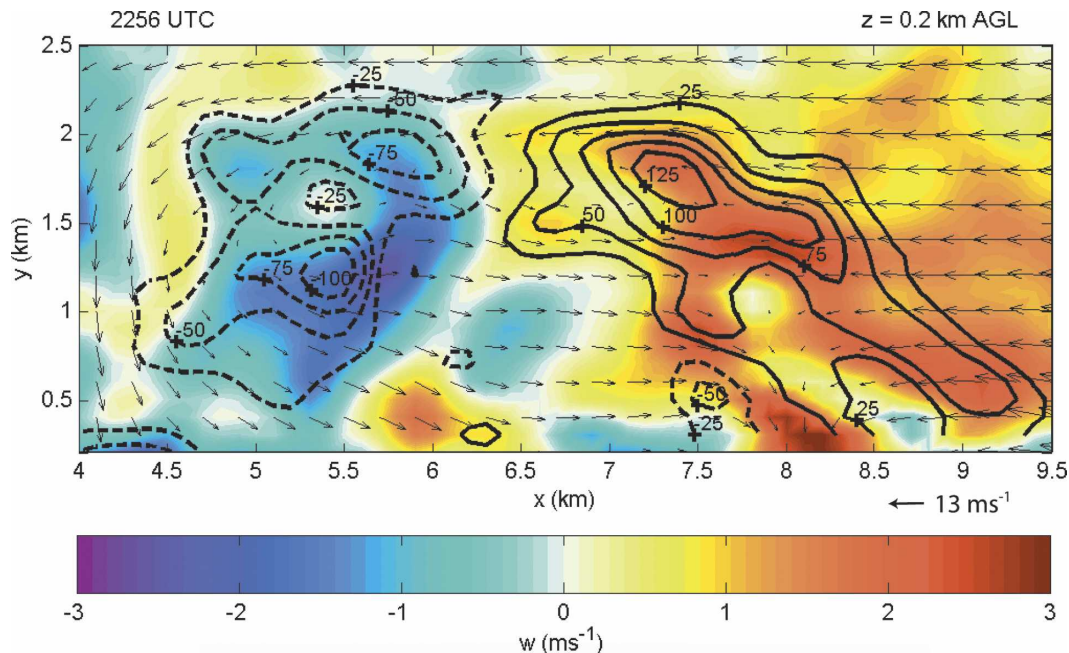


FIG. 11. Same as in Fig. 10, but with contours of stretching (intervals of  $25 \times 10^{-6} \text{ s}^{-2}$ ). Solid contours denote positive stretching, while dashed contours denote negative stretching. Wind vector length equal to grid spacing is  $6.5 \text{ m s}^{-1}$  (every other grid point is shown).

the Del City/Fort Cobb and McLean storms is within the inflow. Therefore, while it is possible for tornadogenesis to proceed with some crosswise horizontal vorticity in the downdraft, it is likely that a large component of crosswise horizontal vorticity throughout the low levels of a supercell, such as that seen in the Kress storm, inhibits tornadogenesis, and could have contributed to the preclusion of tornadogenesis during the analysis time.

In addition to the limitation of surface mesocyclonic strength caused by a large component of crosswise horizontal vorticity, another possibility is that of a relatively cool RFD. Markowski et al. (2003) showed that RFDs containing relatively cool air are more likely to produce low-level stagnation once air reaches the surface. Warmer air, with decreased centrifugal forces and more positive buoyancy, favors the production of a stronger low-level vortex, owing to increased concentration of angular momentum. In a similar, but solely kinematic study, Trapp (1997) suggested that nontornadic mesocyclones have larger core radii and are associated with weaker low-level vertical vorticity than tornadic mesocyclones.

Application of these theories to the Kress storm is an intriguing possibility. Mesocyclones observed within the Kress storm were markedly larger and less organized near the surface than aloft (cf. the  $10 \times 10^{-3} \text{ s}^{-1}$  contour between the surface and 1.6 km AGL in Fig. 6).

Broad rotation near the ground was present throughout the synthesis time period and did not contract or intensify. Many volumes contained surface mesocyclones that struggled to maintain their individual circulations (Figs. 6 and 9). If the RFD air was relatively cool, the convergence capability of the low-level vortices would have been limited. However, without thermodynamic measurements, it is impossible to assess temperature characteristics.

#### e. Forward-flank reflectivity gradient structure

As described above, the vertical structure of the forward-flank reflectivity gradient is rather unconventional. Typically, given a cold pool within the forward flank, gust front formation occurs along the baroclinic zone separating the cool air underneath the forward flank and the warmer air within the inflow region. Such a case would show the strongest convergence near the ground, as cool air descending within the forward flank diverges upon reaching the surface. However, at the time of the synthesis, the Kress storm shows the inverse of this situation. Not only was there almost an absence of a surface forward-flank gust front (or up to  $\sim 0.5$  km AGL for that matter), the gust front strengthened with height up to the vertical limit of the synthesis. Figure 12 shows a cross section through the reflectivity gradient along the forward flank of the Kress storm. The  $\mathbf{V}/\mathbf{W}$

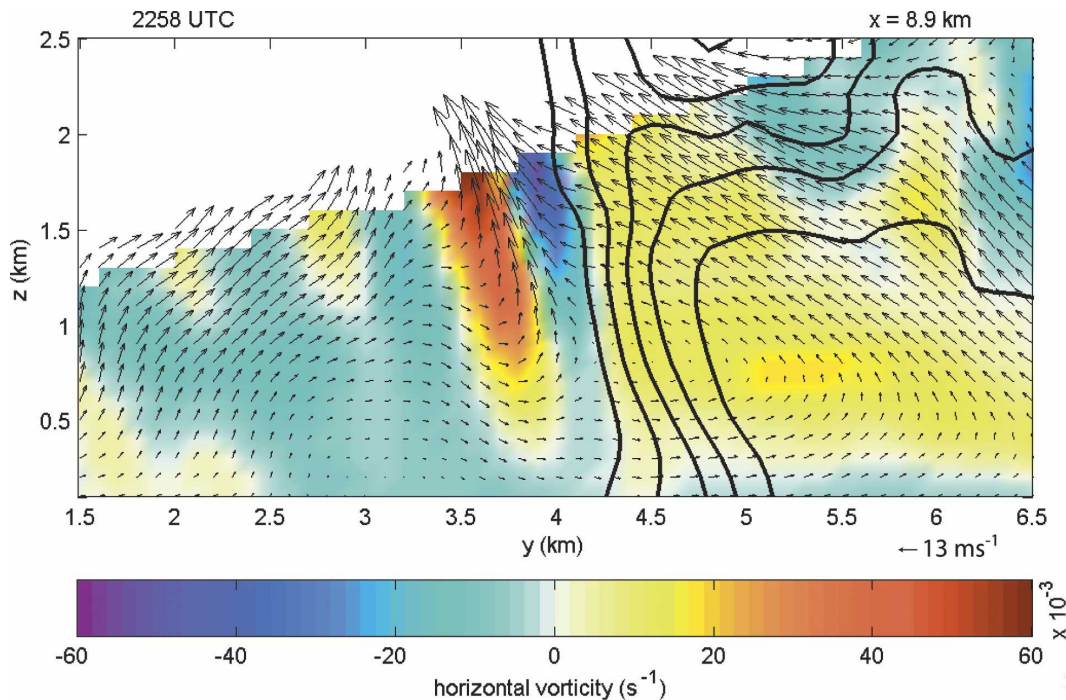


FIG. 12. Vertical ( $Y$ - $Z$ ) cross section through the forward-flank reflectivity gradient at 2258 UTC. Contours of reflectivity exist at 30, 35, 40, 45, and 50 dBZ. Also shown are  $\mathbf{V}/W$  storm-relative wind vectors and the  $x$  component of horizontal vorticity in color (positive horizontal vorticity is directed out of the page). Wind vector length equal to grid spacing is  $6.5 \text{ m s}^{-1}$  (every other grid point is shown).

wind vectors near the surface show no signs of convergence. Above 0.5 km AGL, the first signs of convergence can be seen. This result is in agreement with the vertical structure analysis described before.

The horizontal vorticity associated with the forward-flank convergence zone is also not typically what would be expected with a forward-flank gust front. Traditionally, solenoidal generation of horizontal vorticity is thought to produce resultant horizontal vorticity directed toward the mesocyclone. However, without any negative vertical velocity within the southern portion of the forward flank of the Kress storm, the convergence between the inflow and the forward-flank air resulted in a couplet of horizontal vorticity at the convergence zone (Fig. 12). Just north of the convergence zone, horizontal vorticity was directed toward the west, while directly south of the boundary, it was oriented toward the east. Also, notice the broad region of horizontal vorticity that was directed toward the east both within the forward flank and within the reflectivity gradient along the southern portion of the forward flank. The orientation of this secondary area of horizontal vorticity is also the opposite of what is typically expected.

Throughout the region depicted in this cross section, the  $U$  component of the wind was from the east, suggesting that the couplet of horizontal vorticity south of

the forward-flank reflectivity gradient may have eventually interacted with mesocyclones farther west. The possible effects of these counterrotating vorticity tubes on the mesocyclones, if they were ingested, are unknown. Trajectories are needed to verify the advection of this vorticity as well as if and where tilting and/or stretching was altering the orientation of the vorticity.

This observed vertical structure may suggest that the forward-flank gust front associated with the Kress storm during the time of the syntheses could have origins of a more dynamic than thermodynamic nature. While not contained within the dual-Doppler syntheses, a strong midlevel anticyclonic circulation found in other studies (e.g., Dowell and Bluestein 1997) existed aloft within the northern rear-flank of the Kress supercell and was visible in single-Doppler data. The strength of this circulation increased with height, resulting in increasingly northerly flow within the forward flank of the storm. This flow pattern combined with veering of the environmental inflow with height may have helped to provide this convergence.

It is important to note that this analysis represents only a snapshot of the dynamics of the Kress storm at this time. Although the Kress storm was mature at the time of the syntheses and lacked a distinct surface forward-flank gust front, its formation at a later point is

possible, given the dramatic dynamical evolution occurring within the storm.

#### f. Hook echo evolution and deformation analysis

With each successive mesocyclone, a hook echo decay and regeneration process occurs. This process has not been well documented in past literature. Previous cyclic studies have focused on the dynamics and evolution of the mesocyclones themselves, neglecting the hook echo. It is evident that occlusion of the initial mesocyclone also drives a migration of the old hook echo toward the north in the direction of the forward flank, while a newly formed tendril of precipitation migrates cyclonically around a newly formed mesocyclone.

The process of hook echo regeneration appears to rely in part on advection at low levels. At the time of Fig. 13, a new hook echo had begun to reform around mesocyclone 3, with qualitative evidence that an axis of confluence and convergence (CC) closely paralleled the hook echo in reflectivity. One area of CC existed east of mesocyclone 2, associated with inflow winds and flow from the northern portions of mesocyclone 3 encroaching on winds around mesocyclone 2. Advection associated with this area of CC likely caused the old hook echo to migrate toward the north during occlusion. In addition, another area of distinct CC existed west of mesocyclone 3, where northerly flow dominated. The wind field in this region was shaped by air from the newly formed mesocyclone 3 impinging on westerly momentum both from the RFD and from the southern portion of mesocyclone 2. This secondary area of CC acted to channel rain and hail falling from aloft into a narrow tendril that was then advected cyclonically around the newly developed mesocyclone. These flow patterns may imply that the full formation of the new mesocyclone is necessary before these areas of CC can exist, and therefore before conventional hook echo regeneration can take place.

The relative positions of occluded and newly developed mesocyclones appear to have an effect on the structure and evolution of hook echo redevelopment. In storms not cycling as rapidly as the Kress storm, a new mesocyclone may not be positioned as close to an occluded mesocyclone, limiting the strength of CC. Therefore, the distance between successive mesocyclones could potentially play a role in the speed of the regeneration process. Another possibility can be seen in the last cycle of the Kress storm, where the incomplete mesocyclone 4 developed too close to mesocyclone 3 to contain a fully developed circulation. This close proximity appeared to have had an effect on hook echo regeneration as can be seen in the last seven images of Figs. 7 and 8. Instead of the process described

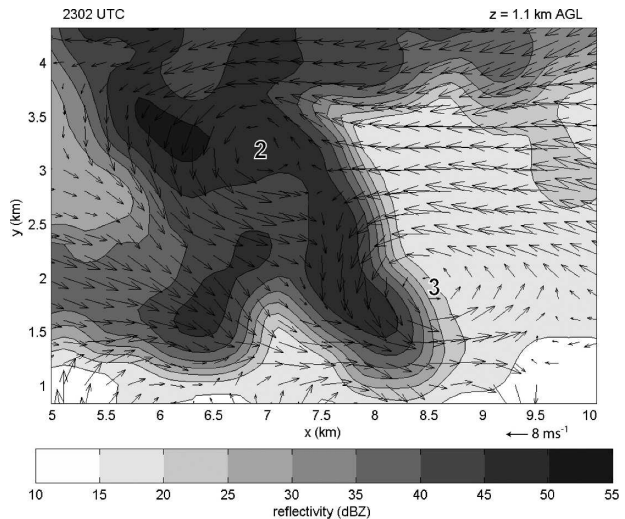


FIG. 13. Horizontal cross section of reflectivity and storm-relative horizontal wind vectors at 1.1 km AGL from 2302 UTC. Hook echo regeneration was occurring around the newly formed mesocyclone 3. Wind vector length equal to one grid spacing is  $4 \text{ m s}^{-1}$  (every other grid point is shown). Mesocyclones are numbered.

above, the old hook echo wrapped cyclonically through mesocyclone 3 (Figs. 7g,h and 8g,h) and continued in a counterclockwise fashion until reaching its original position, forming the “new” hook echo. The end result in Figs. 7l and 8l is almost identical to the original hook echo orientation in Figs. 7f and 8f.

Wind vector evolution associated with hook echo redevelopment qualitatively appeared to be a possible deformation zone (Fig. 13). This region exists between mesocyclones 2 and 3 where RFD outflow meets inflow air along an east–west axis, while a north–south axis exists, delineating air moving toward both mesocyclones 2 and 3. To assess the structure of the wind field in this region, a deformation calculation was conducted as previously described.

Figure 14 shows a series of images from four different volumes of the Kress storm. Strong deformation (up to  $0.25 \text{ s}^{-1}$ ) is associated with areas northeast, east, and southeast of the old hook echo associated with mesocyclone 2 (Fig. 14a). Deformation northeast and east of mesocyclone 2 resulted in some precipitation being advected north along an axis of dilatation associated with the occluding hook echo ( $x = 6.5, y = 3$  in Fig. 14b). Note that the position of this deformation in Fig. 4b resides within the core of the occluded hook echo in Fig. 4c. Areas of deformation east and southeast of mesocyclone 2 directed hydrometeors along the same axis of dilatation, but in the opposite direction, forming the new hook echo associated with mesocyclone 3 (Figs. 14c,d).

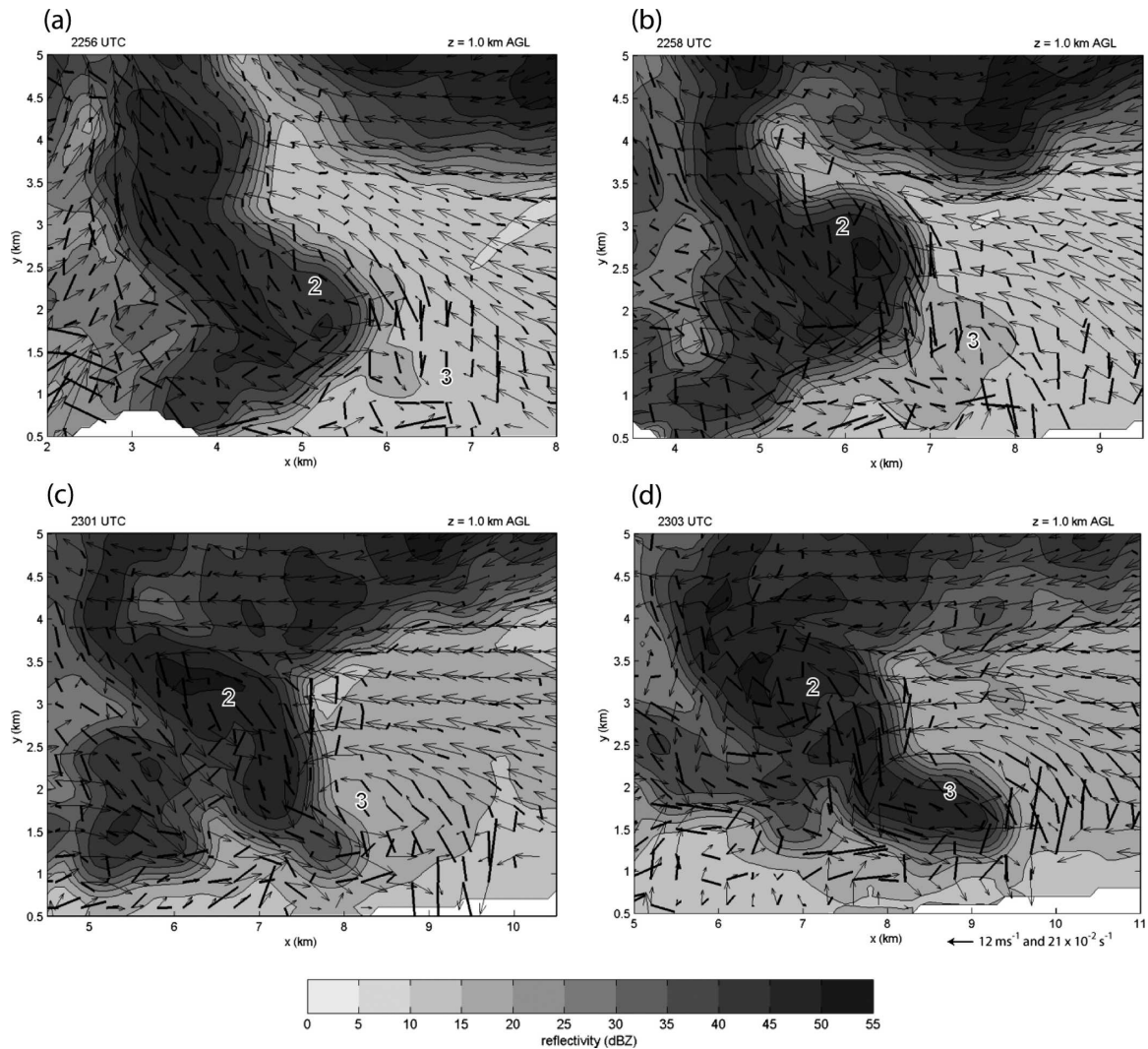


FIG. 14. Horizontal cross section of reflectivity, storm-relative horizontal wind vectors, and deformation tick marks at 1.0 km AGL from (a) 2256, (b) 2258, (c) 2301, and (d) 2303 UTC. Deformation tick marks associated with hook echo reformation are located northeast, east, and southeast of the occluded mesocyclones. Wind vector length equal to one grid spacing is  $4 \text{ m s}^{-1}$  (every third grid point is shown) and deformation tick mark length equal to one grid spacing is  $7 \times 10^{-2} \text{ s}^{-1}$ .

Horizontal advection of precipitation similar to that in the Kress storm has been previously hypothesized as a driving force for hook echo formation in other studies (Fujita 1958; Brandes 1977a; Klemp et al. 1981). However, it is important to note that this should not serve as the only explanation for hook echo formation. There is also evidence within the Kress syntheses of significant negative vertical advection occurring throughout the hook echo, essentially collocated with the RFD. Similar findings have been made in which the hook echo appeared to form due to rain curtains descending within the RFD (Forbes 1981; Adlerman et al. 1999; Markowski 2002). As discussed in Markowski (2002), it appears likely there is more than one mechanism at work during hook echo formation.

A simple conceptual model of the hook echo regeneration process that occurred within the context of cyclic evolution of the Kress storm during the synthesis time period can be seen in Fig. 15. At the onset of the synthesis, deformation contributed to the formation of the initial hook echo, associated with the first mesocyclone (Fig. 15a). In addition, a region of CC associated with the development of a newly formed mesocyclone (labeled “2” in the model), resulted in strong deformation downstream of the initial mesocyclone. As the precipitation filled hook echo encountered this region, small tendrils of hydrometeors were forced both north and south parallel to the axis of dilatation (Fig. 15b). In Fig. 15c, strong deformation associated with CC south of the new mesocyclone prompted more advection of

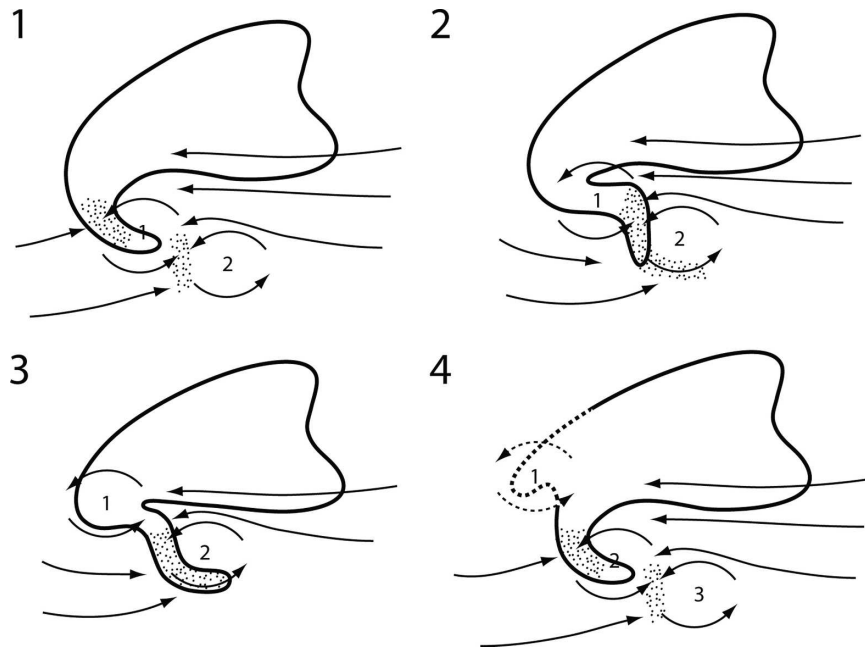


FIG. 15. Idealized low-level conceptual model of cyclic mesocyclogenesis based on observed hook echo regeneration. Radar reflectivity echo of the supercell is outlined with a thick line. Stippled regions depict areas of strong deformation partially responsible for the orientation and evolution of hook echo development. Dashed lines indicate regions with dissipating rotation/organization.

hook echo precipitation around the southern periphery of the vortex. In addition, the initial mesocyclone continued to shift northwestward relative to storm motion. The final phase in this process closely resembled the initial phase; however, the dissipating initial mesocyclone existed with only a small likeness of the original hook echo (Fig. 15d). At this point, both the initial mesocyclone and hook echo are shown using dashed lines to indicate dissolution, as they have become detached from the overall low-level flow. It should be noted that this conceptual model is reliant on the full development of independent successive mesocyclones. Therefore, it does not apply to the last cycle of the Kress storm during the synthesis time period. Finally, this conceptual model does not depict the likely role of negative vertical advection, occurring throughout the hook echo, as well as within the areas of strong deformation, which may have also helped concentrate rainfall into the new hook echo.

### 5. Comparison to previous conceptual models

The mesocyclonic structure of the Kress storm has much in common with previous research concerning both classic supercell models and cyclic processes. The Lemon and Doswell (1979) supercell model describes how the mature mesocyclone becomes disrupted and

develops a divided structure “in which the circulation center lies along the zone separating the rear flank downdraft from the updraft.” This process occurred for both mesocyclones 2 and 3 in the Kress storm. As both mesocyclones matured, they eventually became dominated by downdraft air as the hook echo wrapped through the mesocyclone core during the occlusion process. Adlerman et al. (1999) found model results identifying a similar separation of the occluded mesocyclone from the rear-flank gust front and eventual enveloping of the mesocyclone in precipitation.

The Kress storm contains dynamic cyclic structure that is very similar to the classic Burgess et al. (1982) cyclic mesocyclone model and the modified DB model. According to both the Burgess et al. (1982) and DB models, the initial mesocyclone occludes and moves to the left of the mean storm motion, while the secondary mesocyclone forms along the rear-flank gust front. However, the Kress storm showed secondary mesocyclogenesis occurring in the absence of any forward-flank gust front, in contrast to the Burgess et al. (1982) model, but in agreement with the DB model. This cycle then repeats with the third mesocyclone forming along the rear-flank gust front associated with the second mesocyclone. The culmination of this scenario can be seen in the Kress storm at 2256 UTC and is almost identical to the cyclic structure at time  $t_o + 2\Delta t$  of Fig. 13 in DB02a.

While the dynamics of cyclic structure and location of the mesocyclones within the Kress storm correlated very well with the DB model, the locations of updrafts and downdrafts were not as similar. While two of the mesocyclones from the Kress storm showed portions of positive vertical velocity well after occlusion, all mesocyclones during occlusion were completely engulfed in downdraft air. Both Adlerman et al. (1999) and the DB model maintain a well-formed updraft within the mesocyclone during and after occlusion.

Low-level areas of tilting and subsequent stretching within the Kress storm were somewhat similar to the DB model. However, due to a large component of crosswise horizontal vorticity within the Kress storm, the strongest updrafts of the Kress supercell were offset from the maxima in tilting, while the DB model indicated a stronger correlation between maxima in updraft strength, tilting, and subsequent stretching. In addition, due to the negative vertical velocity evident within each Kress mesocyclone during occlusion, stretching term values became negative, unlike the DB model.

Perhaps one of the biggest differences between either the Burgess et al. (1982) or DB model and the Kress storm during the time of the synthesis is the forward-flank gust front. Both conceptual models indicate its presence, with the DB model indicating a forward-flank gust front of diminished intensity. The Kress storm showed evidence of a forward-flank gust front aloft, but 1–3 km north of the newly developing mesocyclones at levels well above the surface. Therefore, low-level mesocyclogenesis was possible within the Kress storm without any baroclinic effects from the forward flank. This result is similar to the findings of DB, which showed low-level mesocyclogenesis occurring from the tilting and stretching of environmental and storm-modified horizontal vorticity. In addition, the general absence of a surface forward-flank gust front as well as mean ascent within the forward flank could imply the lack of a low-level cold pool during the time of the synthesis. However, both modeling studies of Rotunno and Klemp (1985) and Adlerman et al. (1999) contained cold pools without a forward flank wind shift, suggesting that if a cold pool existed within the forward flank of the Kress supercell at the time of the synthesis, the observed ascent was forced. Without in situ measurements within the Kress storm, a thermodynamic retrieval may be the only way to assess whether or not a cold pool existed.

Another feature of the Kress storm that differs from previous research is the cycling frequency. As mentioned previously, analysis shows that the period of time between successive mesocyclones was about 6 min. This time period is drastically shorter than any

previous study. Adlerman et al. (1999) documented a frequency of about one cycle per 60 min. Burgess et al. (1982) found that initial mesocyclones had a life cycle of around 80 min, with successive mesocyclones lasting 60 min each. In their study, DB found a period of only about 20 min between cyclic tornadoes of the 8 June 1995 McLean storm and Johnson et al. (1987) found a similar time between cycles with the 20 May 1977 Fort Cobb storm.

Adlerman and Droegemeier (2002b) found that the resolved cycling frequency of a modeled cyclic supercell is sensitive to a number of physical as well as computational parameters. In particular, modest decreases in both horizontal and vertical grid spacing can cause a nearly steady-state supercell to undergo relatively rapid cyclic mesocyclogenesis. It is certainly possible that numerical models have previously lacked sufficient resolution to adequately resolve the true cyclic evolution of certain supercells. Similarly, consideration should also be given to the possibility that some past observational studies may have suffered from aliasing in terms of cyclic frequency calculation due to the spatial and temporal resolution of older radar platforms.

Regardless of the frequency, it is likely that the primary forces involved in the periodicity of cyclic mesocyclogenesis are the inflow and outflow strength (DB). As found in tornado 4 of DB02b, if inflow and outflow strength are relatively equal, the low-level mesocyclone/tornado remains in a favorable region of the storm for development. There is evidence from the Kress storm that westerly momentum associated with the RFD was fairly strong during the early part of the synthesis time period, even though vertical velocities within the RFD were not as strong. Storm motion was also relatively slow, enabling the rear-flank gust front to surge well ahead of successive mesocyclones. Applying these findings to those of DB, the observed rapid cycling frequency may have limited the ability of each low-level mesocyclone to reach appreciable values of vertical vorticity, potentially precluding tornadogenesis.

## 6. Conclusions

The Kress DOW dual-Doppler synthesis represents the first ground-based high-resolution (100-m grid spacing) analysis of a supercell. The storm exhibited cyclic mesocyclogenesis, enabling comparison of cyclic structure between this storm and other studies of cyclic supercells, yet it was also nontornadic during the synthesis time period (while it did produce a number of tornadoes later in the evening). Previous cyclic research (DB; Johnson et al. 1987; Adlerman et al. 1999) was focused on supercells that produced tornadoes; there-

fore, a comparison of features between the Kress storm and other tornadic storms provided the opportunity to assess differences/similarities between nontornadic and tornadic supercells.

Dynamic and cyclic processes consistent with previously studied tornadic supercells were shown to apply to the Kress supercell during the nontornadic synthesis time period. These processes include the formation, maturation, dissipation, and structure of discrete mesocyclones. Specifically, the cyclic tornadogenesis conceptual model of DB compared very well to mesocyclonic events during the synthesis time period of the Kress storm. This result likely implies that nontornadic cyclic supercells, beyond the studied storm, can also exhibit similar cyclic processes as tornadic cyclic supercells. This evidence adds to previous research suggesting there is minimal dynamic difference between nontornadic and tornadic supercells (e.g., Trapp 1999; Wakimoto and Cai 2000; Markowski et al. 2002).

However, a number of differences were found between the structure of the Kress storm at the time of the synthesis and previous studies. The cycling frequency was faster than any other supercell studied, either observationally or numerically. An average of  $\sim 6$  min per cycle was found. Along with the broad westerly momentum seen on the southwestern flank of the storm during the beginning of the synthesis, slow storm motion ( $\sim 5 \text{ m s}^{-1}$ ) may have allowed the rear-flank gust front to surge well ahead of each mesocyclone, spurring rapid cyclic development. A hook echo regeneration pattern was found to occur coincident with (and dependent upon the speed of) cyclic mesocyclogenesis and was documented in a conceptual model relevant for the time period of the synthesis. Deformation appeared to play a large role in this process and has proven to be quite useful as an analysis tool toward a better understanding of hook echo structure and evolution.

Another major difference between the Kress storm and previously studied cyclic storms was the structure of the forward-flank gust front, which was almost nonexistent below  $\sim 0.5$  km AGL. Instead, a convergence zone containing a couplet of opposing horizontal vorticity existed and intensified with height above this level. On a related note, a majority of positive vertical velocity existed within the observable portion of the forward flank, making the existence of a cold pool beneath this portion of the forward flank questionable. If a cold pool existed, the vertical motion within the forward flank would have been forced. This lends credence to the possibility that the convergence zone associated with the forward-flank reflectivity gradient may have originated from a more dynamic rather than thermodynamic nature.

The forward-flank gust front was observed to have no impact on the development of successive low-level mesocyclones due to its location in relation to the mesocyclones, and height above the ground. However, it is likely that the elevated gust front influenced mature to occluded mesocyclones in some way. How the couplet of opposing horizontal vorticity affected these mesocyclones is unknown. While the forward-flank gust front had no impact on developing mesocyclones, the rear-flank gust front played a major role in mesocyclogenesis. Tilting and stretching of horizontal vorticity occurred along the rear-flank gust front, helping to focus vertical vorticity.

The Kress supercell showed an abundance of crosswise horizontal vorticity for all regions of the low-level mesocyclone within 800 m of the ground. This may have prevented optimum concentration of horizontal vorticity into the vertical, limiting the strength of low-level circulations both within the downdraft and inflow regions of the storm. It is also possible that the rapidity of cycling may be directly correlated with the success or failure of tornadogenesis (DB), and may have played a role in the nontornadic nature of the Kress storm during the syntheses by limiting the time available for mesocyclone development.

While it is not physically possible to assess due to domain limitation, it would be interesting to evaluate the midlevel updraft structure of the Kress storm, due to the rapidly surging rear-flank gust front. Future high-resolution dual-Doppler analyses with sufficient vertical extent may be able to contribute to a better understanding of low- to midlevel updraft structural interaction. In addition, future analysis of how cycling frequency affects tornadogenesis may be an important step toward learning how the complex interaction of inflow and outflow affects tornadic development.

*Acknowledgments.* This research was supported by NIST (Department of Commerce NIST/TTU Cooperative Agreement Award 70NANB8H0059) and NSF (NSF-ATM-0437505). Curtis Alexander provided valuable assistance for editing and processing techniques and Yvette Richardson contributed to insightful discussions concerning the analysis. David Dowell provided helpful comments and input and aided with deformation calculations. Both Herb Stein and David Dowell supplied excellent video documentation of the Kress supercell during the dual-Doppler deployment. Gordon Carrie provided help with the ViSky software package. The constructive comments and suggestions from two anonymous reviewers were also greatly appreciated. Finally, thanks are due to all who participated and helped collect data from this case during the DOW ROTATE season of 2001.

## REFERENCES

- Adlerman, E. J., and K. K. Droegemeier, 2002a: A numerical simulation of cyclic tornadogenesis. Preprints, *20th Conf. on Severe Local Storms*, Orlando, FL, Amer. Meteor. Soc., 591–594.
- , and —, 2002b: The sensitivity of numerically simulated cyclic mesocyclogenesis to variations in model physical and computational parameters. *Mon. Wea. Rev.*, **130**, 2671–2691.
- , —, and R. Davies-Jones, 1999: A numerical simulation of cyclic mesocyclogenesis. *J. Atmos. Sci.*, **56**, 2045–2069.
- Alexander, C. R., and J. Wurman, 2005: The 30 May 1998 Spencer, South Dakota, storm. Part I: The structural evolution and environment of the tornadoes. *Mon. Wea. Rev.*, **133**, 72–97.
- Barnes, S. L., 1964: A technique for maximizing details in numerical weather map analysis. *J. Appl. Meteor.*, **3**, 396–409.
- Bluestein, H. B., 1977: Synoptic-scale deformation and tropical cloud bands. *J. Atmos. Sci.*, **34**, 891–900.
- Brandes, E. A., 1977a: Flow in a severe thunderstorm observed by dual-Doppler radar. *Mon. Wea. Rev.*, **105**, 113–120.
- , 1977b: Gust front evolution and tornado genesis as viewed by Doppler radar. *J. Appl. Meteor.*, **16**, 333–338.
- , 1984: Relationships between radar derived thermodynamic variables and tornadogenesis. *Mon. Wea. Rev.*, **112**, 1033–1052.
- , 1993: Tornadic thunderstorm characteristics determined with Doppler radar. *The Tornado: Its Structure, Dynamics, Prediction, and Hazards, Geophys. Monogr.*, No. 79, Amer. Geophys. Union, 143–159.
- Burgess, D. W., V. T. Wood, and R. A. Brown, 1982: Mesocyclone evolution statistics. Preprints, *10th Conf. on Severe Local Storms*, Omaha, NE, Amer. Meteor. Soc., 422–424.
- Carbone, R. E., M. J. Carpenter, and C. D. Burghart, 1985: Doppler radar sampling limitations in convective storms. *J. Atmos. Oceanic Technol.*, **2**, 357–361.
- Darkow, G. L., and J. C. Roos, 1970: Multiple tornado producing thunderstorms and their apparent cyclic variations in intensity. Preprints, *14th Conf. on Radar Meteorology*, Tucson, AZ, Amer. Meteor. Soc., 305–308.
- Darkow, J. M., 1971: Periodic tornado production by long-lived parent thunderstorms. Preprints, *Seventh Conf. on Severe Local Storms*, Kansas City, MO, Amer. Meteor. Soc., 214–217.
- Davies-Jones, R. P., 1984: Streamwise vorticity: The origin of updraft rotation in supercell storms. *J. Atmos. Sci.*, **41**, 2991–3006.
- , and H. E. Brooks, 1993: Mesocyclogenesis from a theoretical perspective. *The Tornado: Its Structure, Dynamics, Prediction, and Hazards, Geophys. Monogr.*, No. 79, Amer. Geophys. Union, 104–114.
- Dowell, D. C., and H. B. Bluestein, 1997: The Arcadia, Oklahoma, storm of 17 May 1981: Analysis of a supercell during tornadogenesis. *Mon. Wea. Rev.*, **125**, 2562–2582.
- , and —, 2002a: The 8 June 1995 McLean, Texas, storm. Part I: Observations of cyclic tornadogenesis. *Mon. Wea. Rev.*, **130**, 2626–2648.
- , and —, 2002b: The 8 June 1995 McLean, Texas, storm. Part II: Observations of cyclic tornadogenesis. *Mon. Wea. Rev.*, **130**, 2649–2670.
- Forbes, G. S., 1981: On the reliability of hook echoes as tornado indicators. *Mon. Wea. Rev.*, **109**, 1457–1466.
- Fujita, T. T., 1958: Mesoanalysis of the Illinois tornadoes of 9 April 1953. *J. Meteor.*, **15**, 288–296.
- Heymsfield, G. M., 1978: Kinematic and dynamic aspects of the Harrah tornadic storm analyzed from dual-Doppler radar data. *Mon. Wea. Rev.*, **106**, 233–254.
- Huschke, R. E., Ed., 1959: *Glossary of Meteorology*. Amer. Meteor. Soc., 638 pp.
- Johnson, K. W., P. S. Ray, B. C. Johnson, and R. P. Davies-Jones, 1987: Observations related to the rotational dynamics of the 20 May 1977 tornadic storms. *Mon. Wea. Rev.*, **115**, 2463–2478.
- Klemp, J. B., R. Rotunno, and P. S. Ray, 1981: Observed and numerically simulated structure of a mature supercell thunderstorm. *J. Atmos. Sci.*, **38**, 1558–1580.
- Koch, S. E., M. desJardins, and P. J. Kocin, 1983: An interactive Barnes objective map analysis scheme for use with satellite and conventional data. *J. Climate Appl. Meteor.*, **22**, 1487–1503.
- Leise, J. A., 1982: A multidimensional scale-telescoped filter and data extension package. NOAA Tech. Memo. ERL WPL-82, 19 pp. [Available from NOAA ERL, 325 Broadway, Boulder, CO 80303.]
- Lemon, L. R., and C. A. Doswell, 1979: Severe thunderstorm evolution and mesocyclone structure as related to tornadogenesis. *Mon. Wea. Rev.*, **107**, 1184–1197.
- Markowski, P. M., 2002: Hook echoes and rear-flank downdrafts: A review. *Mon. Wea. Rev.*, **130**, 852–876.
- , J. M. Straka, and E. N. Rasmussen, 2002: Direct surface thermodynamic observations within the rear-flank downdrafts of nontornadic and tornadic supercells. *Mon. Wea. Rev.*, **130**, 1692–1721.
- , —, and —, 2003: Tornadogenesis resulting from the transport of circulation by a downdraft: Idealized numerical simulations. *J. Atmos. Sci.*, **60**, 795–823.
- Miller, L. J., and S. M. Fredrick, 1998: Custom Editing and Display of Reduced Information in Cartesian space (CEDRIC) manual. National Center for Atmospheric Research, Mesoscale and Microscale Meteorology Division, Boulder, CO, 130 pp.
- Oye, R., C. Mueller, and S. Smith, 1995: Software for radar translation, visualization, editing, and interpolation. Preprints, *27th Conf. on Radar Meteorology*, Vail, CO, Amer. Meteor. Soc., 359–361.
- Rotunno, R., and J. B. Klemp, 1985: On the rotation and propagation of simulated supercell thunderstorms. *J. Atmos. Sci.*, **42**, 271–292.
- Schroeder, J. L., W. S. Burgett, K. B. Haynie, I. Sonmez, G. D. Skwira, A. L. Doggett, and J. W. Lipe, 2005: The West Texas Mesonet: A technical overview. *J. Atmos. Oceanic Technol.*, **22**, 211–222.
- Trapp, R. J., 1997: Some quantitative and qualitative characteristics of six storms observed during VORTEX. Preprints, *28th Conf. on Radar Meteorology*, Austin, TX, Amer. Meteor. Soc., 522–523.
- , 1999: Observations of nontornadic low-level mesocyclones and attendant tornadogenesis failure during VORTEX. *Mon. Wea. Rev.*, **127**, 1693–1705.
- Wakimoto, R. M., and H. Cai, 2000: Analysis of a nontornadic storm during VORTEX 95. *Mon. Wea. Rev.*, **128**, 565–592.
- Wicker, L. J., and R. B. Wilhelmson, 1995: Simulation and analysis of tornado development and decay within a three-dimensional supercell thunderstorm. *J. Atmos. Sci.*, **52**, 2675–2703.
- Wurman, J., 2001: The DOW mobile multiple Doppler network. Preprints, *30th Int. Conf. on Radar Meteorology*, Munich, Germany, Amer. Meteor. Soc., 95–97.
- , J. M. Straka, E. N. Rasmussen, M. Randell, and A. Zahrai, 1997: Design and deployment of a portable, pencil-beam, pulsed, 3-cm Doppler radar. *J. Atmos. Oceanic Technol.*, **14**, 1502–1512.